CHAPTER 3

Advances in Aberration-Corrected Scanning Transmission Electron Microscopy and Electron Energy-Loss Spectroscopy

Ondrej L. Krivanek, Niklas Dellby, Robert J. Keyse, Matthew F. Murfitt, Christopher S. Own, and **Zoltan S. Szilagyi***

Contents

I. INTRODUCTION

The properties of electron lenses depend on the distributions of magnetic or electric fields in the space between the lens pole pieces. The fields are subject to the constraints of the Laplace equation and cannot be shaped arbitrarily. This results in conventional round lenses that have unavoidable

* Nion Co., Kirkland, WA 98033, USA

Advances in Imaging and Electron Physics, Volume 153, ISSN 1076-5670, DOI: 10.1016/S1076-5670(08)01003-3.

spherical and chromatic aberrations, whose coefficients are of the same order of magnitude as the focal length of the lenses. This much—plus the fact that abandoning cylindrical symmetry, putting charge on axis, using electron mirrors, or working with time-varying fields can lead to optical systems able to correct the aberrations—has been known for some 60 years. Much of the progress was due to the work of Scherzer (1936, 1947); see also Zworykin *et al*. (1945) for a description of early work in aberration correction.

Aberration-corrected instruments built from 1947 to 1990 typically verified the correction principle, but they failed to improve on the resolution of the best uncorrected instruments. This was the case for correctors built by Seeliger (1953) and Möllenstedt (1956), which followed Scherzer's original designs; correctors that used quadrupoles and octupoles as proposed by Archard (1955) and constructed by Deltrap (1964), Hardy (1967), and the Darmstadt group (Koops, 1978); and the first proof-of-principle sextupole-based corrector of Chen and Mu (1990) that built on the proposals of Beck (1979), Crewe and Kopf (1980), and Rose (1981).

In retrospect, it is clear that several major difficulties impeded improved resolution even after the correction principles were verified experimentally. First, the corrected systems were always more complicated than uncorrected ones and used many more power supplies. The precision needed for these supplies was high, and practical electronics was not able to achieve it until the 1970s. Second, not enough attention was paid initially to parasitic aberrations, which arise due to imperfect materials, limited precision of machining and assembly, and imperfect alignment. The result was that the parasitic aberrations often limited the attainable resolution more severely than the principal aberrations. Third, even when it was realized that parasitic aberrations needed to be characterized and fixed, diagnostic procedures able to quantify them easily and preferably automatically (without direct human intervention) took time to develop. Without such procedures, it was beyond most human operators to set up the instruments as needed.

The situation turned more favorable in the 1990s, largely as a by-product of three developments: (1) the introduction of charge-coupled device (CCD) cameras in electron image recording (Mochel and Mochel, 1986), which made high-quality image data available for immediate computer analysis; (2) the increasing power of personal computers, which allowed the data to be analyzed in real time; and (3) the development of efficient aberration-diagnosing algorithms (e.g., Krivanek *et al*., 1992, 1993, 1994, 1997), which allowed the aberrations to be determined rapidly and accurately. These advances made possible the development of the first successful correctors for the three main types of electron microscopes (EMs) in the space of just 3 years: scanning electron microscopes (SEMs) (Zach and

Haider, 1995a, 1995b); transmission electron microscopes (TEMs) (Haider *et al*., 1998a, 1998b); and scanning transmission electron microscopes (STEMs) (Krivanek *et al*., 1997; Krivanek, Dellby and Lupini, 1999).

The new instruments ushered in a new, "aberration-corrected" era of electron optics. The era is characterized by rapid advances in both the attainable spatial resolution and the analytical sensitivity. Starting from about five aberration-corrected EMs at the turn of the millennium, there are now about 100 such instruments in the world, and their numbers are growing rapidly. Several reviews have been published that describe the principles and history of aberration correction (e.g., Rose, 2003; Crewe, 2004; Hawkes, 2004, 2007, 2008; Krivanek, Dellby and Murfitt, 2008) and the abilities of the corrected instruments (e.g., Lentzen, 2006; Nellist, 2005; Smith, 2008; Varela *et al*., 2005, and this volume).

As key examples of the new capabilities, aberration correction has produced the first directly interpretable sub-Ångstrom resolution EM images (Batson, Dellby and Krivanek, 2002), as well as deep sub-Ångstrom resolution images (Nellist *et al*., 2004). Many new applications using the improved resolution have followed since, as documented in this volume. The correction has also improved the attainable contrast levels and thus the visibility of light elements. This has allowed light atoms such as oxygen to be imaged in a CTEM (Jia, Lentzen, and Urban, 2003) and in a STEM using both bright-field (BF) and high-angle annular dark-field (HAADF) modes (Chisholm *et al*., 2004). Correction has also led to greatly increased currents in atom-sized probes. This has resulted in the acquisition of electron energy-loss spectra from single atoms even in an instrument with non-optimized collection optics (Varela *et al*., 2004), and the acquisition of atomic-resolution chemical maps in less than 1 minute in a more recent instrument (Muller *et al*., 2008). The increased probe current and improved resolution have similarly lowered the detection limits of energy-dispersive X-ray spectroscopy (EDXS) close to a single atom (Watanabe *et al*., 2006).

Aberration correction has also initiated a drive toward new EM columns whose stability and flexibility are improved to be in line with the increased performance made possible by the correction (van der Stam *et al*., 2005; Sawada *et al*., 2007; Krivanek *et al*., 2008a). One of the columns was designed "from the ground up" and incorporates major innovations, such as a sample stage that is compensated for temperature variations and is more vibration- and drift-free, and better suited for computer control than typical side-entry stages (Own *et al*., 2006; Krivanek *et al*., 2008b).

This chapter reviews the principles used by aberration-corrected instruments and the performance they should be able to attain. We provide application examples from areas we consider especially promising, and discuss what may be next for aberration-corrected STEM.

II. ABERRATION CORRECTION BY NON-ROUND LENSES

The account of aberration correction optics presented here is a brief one that concentrates on matters of practical interest to scanning transmission electron microscopy. For more thorough reviews of the optics behind aberration correction, see Krivanek, Dellby, and Murfitt (2008) and Hawkes (2008), plus Hawkes (2007) and Hawkes and Kasper (1996) for additional information.

There are many aberrations to correct. Figure 1 shows a graphic representation of the distortions of the electron wavefront that are produced by axial geometric aberrations of up to fifth order, together with the symbols denoting the aberrations. The n index in the $C_{n,m}$ notation system refers to the order of the aberration: the wavefront distortion due to an aberration of nth order increases as the distance of an electron ray from the optic axis in the aperture plane to the $(n+1)$th power, and it displaces the corresponding ray in the image plane as the nth power of the distance. The m index refers to the angular multiplicity: the wavefront distortion due to an aberration of multiplicity m goes through m maxima (and m minima) when the coordinate system is rotated through 360 degrees. The a and b indices account for the fact that azimuthally varying aberrations (all aberrations with $m > 0$) have two orthogonal components, rotated by $\pi/2m$ with respect to each other. The magnitude of each $C_{n,m,a}$ or $C_{n,m,b}$ aberration stands for the strength of the corresponding aberration coefficient.

Quantitatively, the wavefront distortions are described by the aberration function $\chi(\theta,\phi)$, which is defined as the physical distance between the actual wavefront converging on the sample, and an ideal spherical wavefront as

$$\chi(\theta,\phi) = \sum_n \sum_m \{C_{n,m,a}\theta^{n+1}\cos(m\phi) + C_{n,m,b}\theta^{n+1}\sin(m\phi)\}/(n+1), \tag{1}$$

where the sum over n is taken from 0 to the highest order of aberrations of interest, and the sum over m is taken from 0 (or 1) to $n+1$ for each order n, subject to the additional constraint that $m+n$ is odd. The angles θ and ϕ are the polar angular coordinates of a ray converging on the sample. The standard location for defining the aberration function is the front-focal plane of the final probe-forming lens of the STEM (i.e., its objective lens). This plane lies a focal length f in front of the sample, and the transverse positions (x,y) in it are defined, using the paraxial approximation, as $x = f\theta\cos(\phi), y = f\theta\sin(\phi)$. The aberration function also describes the phase shift of each partial ray relative to the central ray traveling along the optic axis, which is given by $\Delta\eta = 2\pi\chi(\theta,\phi)/\lambda$.

See Krivanek, Dellby, and Murfitt (2008) for a more detailed explanation of the notation and of the equation defining the aberration function, and

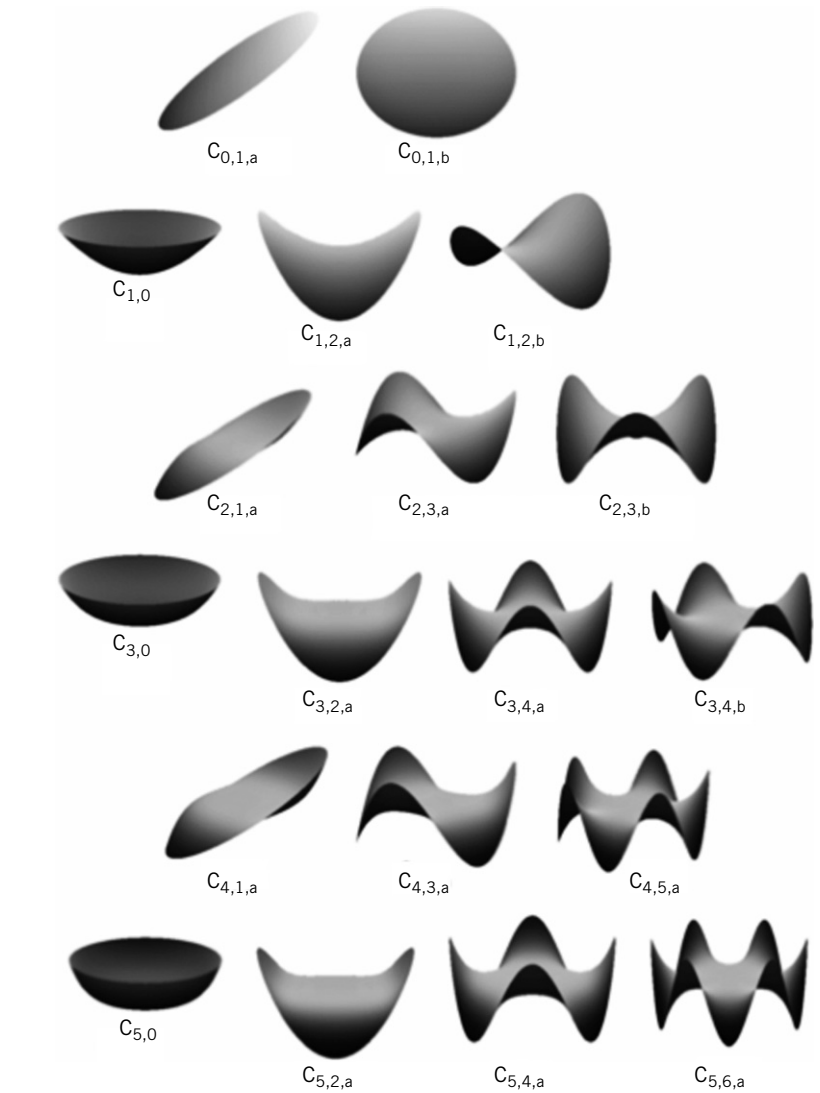

FIGURE 1 Contributions to the aberration function due to aberrations from the zeroth to the fifth order.

Hawkes (2008) for a table comparing the notation used here with other notation systems currently in use. Note also that notation systems that use different letters and different pre-factors for different aberrations do not provide a simple expression for $\chi(\theta, \phi)$ for aberrations up to an arbitrarily high order (e.g., compare Eq. (1) above with equation (2) of Haider *et al*. (2008)) and that expressing the rules linking different aberrations that are discussed below is much more cumbersome in the alternate systems.

In the first electron microscopes, defocus $C_{1,0}$ was the only parameter that could be adjusted freely. The main resolution limit came from the next important aberration: simple twofold astigmatism $C_{1,2}$. This was nulled by the addition of an adjustable stigmator (Bertein, 1947; Hillier and Ramberg, 1947; see Haguenau *et al*., 2003). Axial coma $C_{2,1}$, which arises when systems with spherical aberration are misaligned, emerged as a concern in mainstream electron microscopy in the 1970s (Krivanek, 1978; Zemlin *et al*., 1978). Threefold astigmatism $C_{2,3}$ became a concern in the 1990s after procedures for determining it rapidly were developed (Ishizuka, 1994; Krivanek, 1994; Krivanek and Stadelmann, 1995). With aberration correction, all the terms up to $C_{3,4}$ became a concern for the first practical correctors. The latest correctors now either directly control, or at least keep acceptably small, all aberrations up to $C_{5,6}$ (Krivanek *et al*., 2003; Dellby, Krivanek, and Murfitt, 2006; Müller *et al*., 2006). This illustrates how accelerated the progress has become in the past 10 years.

Figure 1 does not show field-dependent (off-axial) aberrations, because these are usually not limiting in the STEM. When they need to be considered in depth, such as for conventional broad-beam CTEM imaging, they can be readily described as the variation of the axial aberrations across the field of view (Dellby, Krivanek, and Murfitt, 2006; Krivanek, Dellby, and Murfitt, 2008).

Despite the large number of aberrations that need to be dealt with, designers of aberration correctors for TEMs have but a few types of optical elements in their "tool kit": round lenses and various multipoles. The multipoles include dipoles and weak quadrupoles, which were already used in non-aberration-corrected optics, and further strong quadrupoles, sextupoles, and octupoles, and probably higher-order multipoles in future. Round lenses typically only increase the aberrations of the total system. This leaves the task of correcting the many possible aberrations depicted in Figure 1 up to the multipoles.

When multipoles are working in isolation, they can change only a rather limited number of aberrations. A quadrupole, sextupole, and an octupole acting on a non-aberrated round beam only produce twofold astigmatism $C_{1,2}$, threefold astigmatism $C_{2,3,}$and fourfold astigmatism $C_{3,4}$, respectively, as their principal effect. These are only indirectly related to spherical aberration $C_{3,0}$, which limits the resolution in most uncorrected instruments, and to aberrations such as axial coma of second and fourth order ($C_{2,1}$ and $C_{4,1,}$ respectively) and twofold astigmatism of spherical aberration ($C_{3,2}$), which are likely to arise as parasitic aberrations. Precise control of aberrations other than those readily produced by the multipoles acting on a round beam is nevertheless possible because of two fundamental effects produced by optical elements separated along the direction of the electron travel: combination and misalignment aberrations.

Combination aberrations arise when a beam of electrons traverses an optical element producing aberration $C_{n,m}$ and then enters another optical element producing aberration $C_{n',m'}$. When the aberrations are small (i.e., the originally round beam is barely distorted), this combination of events produces aberrations $C_{n+n'-1,m+m'}$ and $C_{n+n'-1,|m-m'|}$, except when both the aberrations are the highest multiplicity ones allowed for a given order ($m = n + 1$, $m' = n' + 1$), in which case only the lower-multiplicity $|m - m'|$ aberration is produced.

As a practical example, combining the effect of two thin sextupoles, each of which produces threefold astigmatism $C_{2,3}$, produces adjustable spherical aberration $C_{3,0}$ ($n = 2 + 2 - 1, m = 3 - 3$) as a combination aberration. The same applies to an extended sextupole, which can be viewed as a succession of thin sextupoles and thus also produces $C_{3,0}$. This is the principle behind sextupole correctors, which use the resultant negative spherical aberration to counteract the positive $C_{3,0}$ ($= C_s$) of the rest of the optical system. (Note that we prefer to adhere to Latin nomenclature and call six-pole optical elements *sextu*poles. If we were to follow Greek nomenclature instead by calling six-pole elements *hexa*poles, for consistency we should then have to call four-pole elements "*tetra*poles.")

As another practical example, combining $C_{3,0}$ produced by a corrector with $C_{3,0}$ produced by the objective lens of a microscope produces an adjustable fifth-order spherical aberration $C_{5,0}$ as a combination aberration. The size of the aberration can be adjusted by moving the two elements relative to each other along the optic axis, or much more practically, by coupling them electron-optically via a set of lenses such that an image of the first element is produced in the vicinity of the second element, and then adjusting the exact position of the image. This principle, proposed by Shao (1988), is used to correct or minimize $C_{5,0}$ in all present-day instruments that correct aberrations higher than third-order.

It is interesting to note that combining octupoles has the same effect: $C_{3,4}$ combined with $C_{3,4}$ also gives adjustable $C_{5,0}$. Correction of $C_{5,0}$ by octupoles was indeed suggested by Rose (1981) and Shao, Beck and Crewe (1988). But because the same effect comes essentially for free in any C_3 corrector properly coupled by first-order optics to an objective lens, using octupoles for $C_{5,0}$ correction has not been explored experimentally.

As two more practical examples, combining $C_{3,4}$ produced in one stage of a correction apparatus with $C_{2,3}$ produced in another stage of the apparatus gives adjustable $C_{4,1}$, and this can be used to adjust fourth-order coma. Combining $C_{3,0}$ with $C_{2,3}$ produces $C_{4,3}$, and it can be used to adjust fourth-order threefold astigmatism. In similar ways, controls for all important parasitic aberrations can be devised and implemented.

As a final example, combining $C_{2,3}$ produced by the strong sextupoles in a sextupole corrector with $C_{3,0}$ that is itself produced as a combination

aberration in an extended sextupole (and is also present in the round coupling lenses between the sextupoles) gives $C_{4,3}$. Combining this mostly double-combination aberration with the strong $C_{2,3}$ of the sextupoles once more produces $C_{5,0}$ and $C_{5,6}$ as triple-combination aberrations. $C_{4,3}$ is canceled along with $C_{2,3}$ by the second sextupole in a symmetrical sextupole corrector, whereas $C_{5,0}$ and $C_{5,6}$ are doubled. $C_{5,0}$ can be canceled by misprojecting the second sextupole into the objective lens, leaving $C_{5,6}$ as the most important intrinsic aberration of this type of corrector (Shao, 1988; Rose, 1990a; Müller *et al.*, 2006).

When the beam distortion produced by the first optical element is no longer slight, several combination aberrations of the order $n + n' - 1$ are produced. This principle is used by quadrupole-octupole correctors, in which a quadrupole at the corrector's entrance typically produces either a line crossover or an elliptical beam in a subsequent octupole. $n + n' - 1 = 3$ for this case, and an octupole with an elliptical beam in it gives adjustable $C_{3,0}$, $C_{3,2,}$ and $C_{3,4}$. The exact proportions of the aberrations depend on the aspect ratio of the beam ellipse. For a line crossover, the ratios for the three aberrations are $1, 4/3$, and $1/3$, respectively (Krivanek, Dellby, and Brown, 1996)—that is, their magnitudes are comparable. A line crossover rotated by 90 degrees incident on a similar octupole gives coefficients of the same magnitude, with the sign of $C_{3,2}$ is reversed. A pair of octupoles with the same aspect ratio ellipses, but rotated by 90 degrees to each other, therefore gives adjustable $C_{3,0}$ and $C_{3,4}$, whose ratio is determined by the aspect ratio of the ellipse. Adding a third octupole to this system, at a location in which the beam is round, allows the fourfold astigmatism $C_{3,4}$ to be nulled, resulting in a corrector that provides adjustable spherical aberration $C_{3,0}$. This is the correction principle used by quadrupole-octupole correctors, including quadrupole-octupole correctors that also correct fifth-order aberrations (Krivanek *et al.*, 2003; Rose, 2004; Dellby, Krivanek, and Murfitt, 2006).

Misalignment aberrations arise when the electron beam enters an optical element miscentered with respect to its optic axis. They can be viewed more generally as combination aberrations caused by a dipole (which gives rise to a simple deflection $C_{0,1}$) and a more complicated element, but because they are rather ubiquitous, we prefer to put them in a class of their own. For a small miscentering on an element producing $C_{n,m}$ aberration, the principal misalignment aberrations are $C_{n-1,|m-1|}$, plus, when $m < n$, $C_{n-1,\,m+1}$. A miscentered quadrupole acting on a round beam produces an additional deflection ($C_{0,1}$), a miscentered sextupole produces twofold astigmatism $C_{1,2}$, a miscentered octupole produces threefold astigmatism $C_{2,3}$, and a miscentered round lens with spherical aberration $C_{3,0}$ produces axial coma $C_{2,1}$. These effects are used in practice: centering on a sextupole with a round beam in it is used to null twofold astigmatism $C_{1,2}$ in sextupole correctors, centering on an octupole is used to null threefold astigmatism

$C_{2,3}$ in quadrupole-octupole correctors, and centering on a $C_{3,0}$–producing element such as a round lens is used to null axial coma.

Centering on the strong sextupoles used in sextupole–round lens correctors must be particularly precise and stable. In a typical corrector of this type, miscentering the beam on a sextupole by just 3 nm leads to twofold astigmatism that is too large for 50 pm resolution high-angle dark-field imaging and 80 pm resolution BF imaging (Rose, 1981; Krivanek, Dellby, and Murfitt, 2008). This is a direct consequence of the fact that sextupoles excite threefold astigmatism $C_{2,3}$ directly and strongly, whereas $C_{3,0}$ arises only as a second-order effect in them. The threefold astigmatism produced by the first sextupole in a sextupole corrector is rather strong, typically of the order of $C_{2,3} = 0.5$ mm (referred to the objective lens of the microscope). Removing it with sufficient precision thus requires a very accurately aligned second sextupole. No such strong lower-order aberration is first excited and then precisely removed in quadrupole-octupole correctors, in which the astigmatic focusing of the quadrupoles is simply first-order optics arranged differently in two orthogonal directions. It produces alignment tolerances that are no more serious than the tolerances for round lenses in other parts of the system. Quadrupole-octupole correctors of geometric aberrations are therefore less sensitive to misalignment and hence potentially more stable.

III. PERFORMANCE OF ABERRATION-CORRECTED INSTRUMENTS

A. Probe Size and Probe Current

In an aberration-corrected STEM, the smallest attainable probe size depends on a number of factors: the remaining (uncorrected) principal aberrations, the strength of parasitic aberrations (often determined by the precision of the tuning), and the dominant instabilities. The current available in a probe of a given size depends on these factors too, plus the brightness of the electron source. The attainable resolution depends on the probe size, the probe current, and the nature of the sample. Given this degree of complication, it is often difficult to provide an exact expression for what the resolution and/or the probe current will be. Nevertheless, simple formulas for the main factors governing the probe size and current provide useful insights into the limits of aberration-corrected performance.

To work out the resolution limited by geometric aberrations, we adopt the criterion that the optimum convergence semi-angle α of the STEM probe is one for which the wavefront converging on the sample does not deviate by more than $\pm\lambda/8$ from the ideal spherical wavefront. This criterion is slightly stricter than necessary under ideal conditions, but because there

are many aberrations to consider and various small effects will not be taken into account by the present discussion, adopting a stricter criterion is likely to lead to a better overall agreement with experiment.

Before aberration correction, the aberration function $\chi(\theta)$ was dominated by spherical aberration C_s and defocus Δz:

$$\chi(\theta) = C_s\theta^4/4 + \Delta z\theta^2/2, \tag{2}$$

where we are using the conventional symbols for spherical aberration C_s and defocus Δz rather than the equivalent $C_{3,0}$ and $C_{1,0}$ used in the preceding section. The aberration function is rotationally invariant in this simple case. The largest usable probe half-angle α_{geom} for which the aberration function $\chi(\theta)$ stays within a band $\lambda/4$ wide is obtained when

$$\Delta z = -(C_s\lambda)^{1/2}, \alpha_{\text{geom}} = \sqrt{2}\,(\lambda/C_s)^{1/4}. \tag{3}$$

The maximum angle admitted into the probe then determines the geometric probe size (full width at half-maximum, FWHM), as described by the familiar expressions for diffraction-limited resolution:

$$d_{\text{geom}} = 0.61\lambda/\alpha_{\text{geom}} \tag{4a}$$

$$= 0.43C_s^{1/4}\lambda^{3/4}. \tag{4b}$$

Equation (4b) is the same as the expression for BF resolution limited by spherical aberration derived by Scherzer (1949), except that the numerical factor is 1.6× smaller. Note that if we do not compensate for the spherical aberration by adjusting the defocus to optimally oppose it, the aberration function will reach the limiting value already at $\alpha = (\lambda/C_s)^{1/4}$, and the probe size will then be $\sqrt{2}\times$ worse. Choosing the optimal defocus therefore has a similar effect to leaving the defocus at zero and reducing C_s by $(\sqrt{2})^4 = 4\times$.

C_s was typically between 0.5 and 1.0 mm for high-performance uncorrected microscopes, which represents a variation of only 20% when it appears in the fourth root. This meant that the attainable probe size was determined much more by the electron wavelength λ and thus the primary beam energy than by the exact size of the spherical aberration coefficient. Going to a higher energy was therefore the only practical way to attain atomic resolution in uncorrected instruments.

With aberration correction, some things have changed, and some have stayed the same. C_s can now be set to an arbitrarily low value, and other aberrations determine the resolution. There is a large number of aberrations to consider, as shown by Figure 1. The effects of many of the aberrations can

be reduced by adjusting lower-order aberrations to optimum values, similar to the way defocus is used to reduce the effect of spherical aberration. The general rule is that a higher-order aberration can be compensated by lower-order aberrations of the same multiplicity. As an example, twofold astigmatism of seventh-order $C_{7,2}$ can be compensated by $C_{5,2}$, $C_{3,2}$, and regular astigmatism $C_{1,2}$. Not surprisingly, such a large number of lower-order terms allows one to compensate $C_{7,2}$ rather accurately, reducing its effect by up to 110× (Krivanek, Dellby, and Murfitt, 2008). The reduction factor is smaller when fewer lower-order aberrations of the same multiplicity are available for the compensation, and no compensation is possible for maximum multiplicity aberrations such as $C_{1,2}$, $C_{2,3}$, etc., for which no lower-order aberrations of the same multiplicity exist.

The compensation is best described by introducing weighing factors $F_{n,m}$ that show how much the effect of a properly compensated aberration of type $C_{n,m}$ on the aberration function is reduced relative to aberrations that cannot be compensated. The weighing factors also take into account that azimuthally invariant aberrations ($m = 0$) only change the aberration function in a unipolar way, and the range of wavefront deviations they cause is therefore only half of those due to azimuthally varying aberrations (with $m > 0$). The weighing factors are listed in Table I for aberrations up to seventh order.

Note that the different aberrations used to balance each other are typically controlled by separate power supplies, and each one of the aberrations needs to be kept stable enough so that its variation does not distort the wavefront unacceptably. In other words, properly adjusted compensation can be used to accommodate larger aberration coefficients than would be admissible without it, but it has no effect on the stability requirements for each aberration. Fortunately, the stability requirements for higher-order

TABLE I Weighing Factors $F_{n,m}$ for Different Aberration Coefficients

Coefficient	Weighing factor $F_{n,m}$	Coefficient	Weighing factor $F_{n,m}$	Coefficient	Weighing factor $F_{n,m}$
$C_{0,1}$	1	$C_{4,1}$	0.0588	$C_{6,1}$	0.0172
$C_{1,0}$	0.5	$C_{4.3}$	0.132	$C_{6,3}$	0.0263
$C_{1,2}$	1	$C_{4,5}$	1	$C_{6,5}$	0.0909
$C_{2,1}$	0.244	$C_{5,0}$	0.0313	$C_{6,7}$	1
$C_{2,3}$	1	$C_{5,2}$	0.04	$C_{7,0}$	0.0078
$C_{3,0}$	0.125	$C_{5,4}$	0.103	$C_{7,2}$	0.0091
$C_{3,2}$	0.167	$C_{5,6}$	1	$C_{7,4}$	0.0189
$C_{3,4}$	1			$C_{7,6}$	0.0769
				$C_{7,8}$	1

aberrations, some of which can be compensated very successfully, are typically much looser than the requirements for lower-order ones. The requirements therefore almost never present a practical problem even without the help of the compensation.

The maximum probe half-angle for which the range of wavefront distortions remains smaller than $\lambda/4$ in the presence of optimally compensated aberrations of a particular order n is given by

$$\alpha_{\text{geom}} = \left((n+1)\lambda \Big/ \left(8 \sum_m F_{n,m} C_{n,m} \right) \right)^{1/(n+1)}, \tag{5}$$

which leads to a probe size of

$$d_{\text{geom}} = 0.61 \left((8/(n+1)) \sum_m F_{n,m}\, C_{n,m} \right)^{1/(n+1)} \lambda^{n/(n+1)}. \tag{6}$$

For a corrector limited by $C_{5,4}$ (such as the Nion second-generation one, Dellby *et al.*, 2001), $F_{5,4} = 0.103$, and the probe size limit due to geometric aberrations becomes

$$d_{\text{geom}} = 0.44\, C_{5,4}^{1/6}\, \lambda^{5/6}. \tag{7}$$

For a $C_{5,6}$-limited sextupole corrector, $F_{5,6} = 1$, and the geometric aberration limit on the probe size is

$$d_{\text{geom}} = 0.64\, C_{5,6}^{1/6}\, \lambda^{5/6}. \tag{8}$$

For quadrupole-octupole correctors that have $C_{7,0}$ to $C_{7,8}$ of comparable magnitudes as the lowest-order uncorrected principal aberrations (Dellby, Krivanek, and Murfitt, 2006), the resolution is mainly limited by $C_{7,8}$ as

$$d_{\text{geom}} = 0.61\, C_{7,8}^{1/8} \lambda^{7/8}. \tag{9}$$

All the above expressions have a much stronger dependence on the electron wavelength than on the aberration coefficients. This means that decreasing λ by increasing the primary energy E_o will remain an effective path to higher resolution in all aberration-corrected instruments, with the possible exception of geometrically and chromatically corrected ones, for which an optimum primary energy of ~200 keV may exist (Haider *et al.*, 2008).

The electron wavefront is also affected by chromatic aberration effects. The contributions to the probe intensity for electrons of different energies

add up incoherently, and chromatic aberration therefore often preserves a sharp central maximum of the probe while increasing the intensity of the probe tails. A more detailed discussion of this effect is given by Krivanek *et al*. (2008a). The tail increase is largely avoided when the probe semi-angle is limited to

$$\alpha_{\text{chrom}} = 1.2\left(\lambda/\left(C_c\,\delta E/E_o\right)\right)^{0.5}, \tag{10}$$

where δE is the FWHM of the energy spread, and E_0 is the primary energy. This leads to a chromatic limit on the probe size of

$$d_{\text{chrom}} = 0.5\,(\lambda C_c\,\delta E/E_0)^{0.5}. \tag{11}$$

The electron wavelength λ is given by the familiar expression

$$\lambda = h/\left(2m_o eE_o\left(1 + eE_o/\left(2m_o c^2\right)\right)\right)^{0.5}, \tag{12a}$$

$$\lambda/pm = 1226/\left(E_o\left(1 + 0.9785^{*}10^{-6}E_o\right)\right)^{0.5}, \tag{12b}$$

$$= 1226/\sqrt{E_o^{*}}, \tag{12c}$$

where E_o is measured in electron volts and E_o^{*} is the "relativistically corrected" primary energy. The chromatic resolution limit is therefore proportional to $1/E_o$ at low primary energies and to $1/E_o^{3/2}$ at high energies. Using a higher primary energy is thus also an effective strategy for decreasing the chromatic resolution limit.

Because both the geometric and chromatic aberrations require that the angular range of the wavefront incident on the sample be restricted, we simply set the illumination half-angle α_{aber} to correspond to the optimum value for whichever aberration is more limiting. The expected probe size due to the combined effect of aberrations and the projected source size is then calculated as

$$d_p = \left(d_{\text{aber}}^2 + d_{\text{source}}^2\right)^{0.5}, \tag{13}$$

where the sum of squares is appropriate because the two resolution-determining factors combine incoherently.

To determine the projected size of the electron source d_{source} that is needed for a given beam current, we start by noting that the current in the electron probe is given by

$$I_p = B\pi^2 d_{\text{source}}^2\,\alpha^2/4, \tag{14}$$

where B is the brightness of the source, specified as current per unit area per unit solid angle. For a particular desired current I_p, the size of the source projected onto the sample therefore needs to be

$$d_{\text{source}} = 2\left(I_p/B\right)^{0.5}/(\pi\alpha), \tag{15a}$$

or alternately

$$d_{\text{source}} = 2\left(I_p/B_r V_o^*\right)^{0.5}/(\pi\alpha), \tag{15b}$$

where B_r is the "reduced" (or "normalized") brightness $B_r = B/V_o^*$, and V_o^* is the relativistically corrected accelerating voltage. In the absence of deleterious effects of instabilities or space charge effects, B_r is invariant throughout the illumination system, from the electron source all the way to the sample.

Combining Eqs. (13), (15), and (4a) then gives the probe size for a desired current I_p:

$$d_p = \left(1 + 1.1\, I_p/\left(B\lambda^2\right)\right)^{0.5} d_{\text{aber}} \tag{16a}$$

$$= \left(1 + 7.3 \times 10^{17} I_p/B_r\right)^{0.5} d_{\text{aber}}. \tag{16b}$$

These expressions show that the minimum attainable probe size is determined by the aberration characteristics of the optical column, and further that this probe size can only be reached in the limit of zero probe current. At any probe current > 0, the probe size also depends on the actual current value and the gun brightness. Note also that the probe size expressed as above does not explicitly depend on the primary energy, although d_{aber} is usually strongly dependent on it.

At high current values, the brightness-dependent term in Eq. (16) becomes as important as the optical performance of the microscope in determining the probe size. This occurs at probe currents for which $7.3 \times 10^{17} I_p/B_r > 1$, that is for

$$I_p > 1.4 \times 10^{-18} B_r. \tag{17}$$

This simple expression shows that the transition from probes limited mainly by aberrations to probes limited by aberrations and brightness together occurs at a probe current that is the same for all instruments with a given reduced source brightness, i.e. that the transition is independent of the quality of the instrument's optics and of its primary energy.

At this point it is useful to note that the experimental measurement of the electron brightness B (or B_r), that is, the determination of the probe current I_p, illumination half-angle α, the size of the projected source d_{source}, and the

primary voltage V_o, so that B or B_r can be determined using Eq. (14), is not completely straightforward. Determining I_p, α, and V_o is not difficult, but d_{source} can be easily overestimated when using an insufficiently large solid angle at the source, which makes the measured source size appear larger as a result of diffraction-limited imaging, when aberrations arise in the gun part of the optical system that are not accounted for, and when high-frequency vibrations and other instabilities broaden the projected source. The source size can be underestimated when the sharpest detail in a probe is confused with the overall size of the probe, i.e. when the current that ends up in the probe tail is considered as a part of the central maximum.

The generally accepted brightness value for 100 kV cold field emission guns (CFEGs) is $B \sim 1 \times 10^{13}$ A/(m^2 sr), that is, $B_r \sim 1 \times 10^8$ A/(m^2 sr V). However, we typically measure $B_r \sim 2 \times 10^8$ A/(m^2 sr V) for the VG (310) W CFEG. The difference probably arises because we have increased the stability of the gun by improving the stability of its high voltage and deflector coil currents, and because we are careful to align the gun mechanically close to its brightest direction. For Schottky electron guns, the generally accepted values are $B \sim 1 - 5 \times 10^{12}$ A/(m^2 sr) at 100 kV, that is, $B_r \sim 1 - 5 \times 10^7$ A/(m^2 sr V). For example, Müller *et al*. (2006) give $B = 8 \times 10^{12}$ A /(m^2 sr) for a 300-kV Schottky gun, which is equivalent to $B_r = 2.1 \times 10^7$ A/(m^2 sr V).

Figure 2 shows the probe size as a function of the probe current, calculated according to Eq. (16b) for two values of reduced brightness: $B_r = 1.5 \times 10^8$ A/(m^2 sr V) and 3×10^7A/(m^2 sr V), taken here as

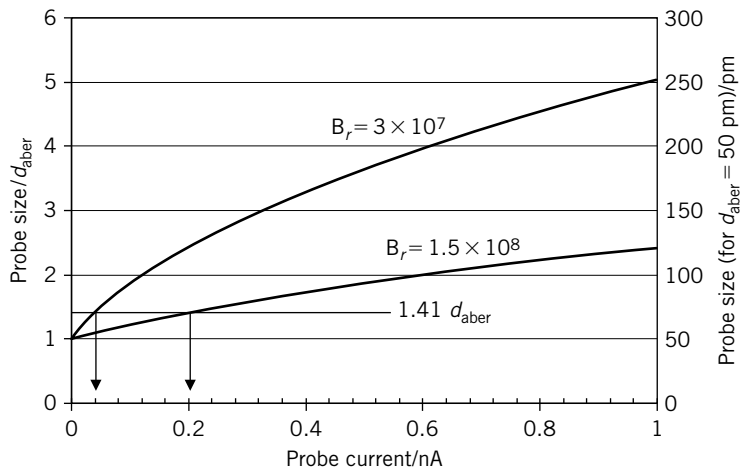

FIGURE 2 STEM probe size d_p as a function of the probe current for two sources of different reduced brightnesses. $B_r = 1.5 \times 10^8$ A/(m^2 sr V) is representative of CFE sources, $B_r = 3 \times 10^7$ A/(m^2 sr V) of Schottky ones. The left-side vertical scale is shown in units of the aberration-limited probe size d_{aber}, the right-side one is in pm for $d_{\text{aber}} = 50$ pm.

representative of CFE and Schottky electron sources, respectively. We have plotted the probe size normalized by d_{aber}, that is, as a general curve describing the growth of the probe size at nonzero currents. The figure shows that the probe size is determined more by the aberration performance of the column than by the source brightness for probe currents less than ~40 pA for Schottky systems and less than ~200 pA for CFEG ones. For probe currents greater than these values, the probe size is determined by the brightness and d_{aber} together.

The figure demonstrates that producing small probes at nonzero probe currents is a two-part undertaking: the aberration-limited probe size d_{aber} needs to be minimized by optimizing the optics design, *and* the source brightness needs to be maximized by optimizing the electron source. Users of practical instruments will point to the importance of a third part: optimizing the (in)stabilities of the total system so that they become less limiting than its fundamental optical performance. Laborious though it is, this part can be improved even after the system is installed and is therefore less stringent than the other two. In the rest of this chapter, we assume that the stabilities have been pushed to the required level.

Table II shows the resolutions and probe currents calculated using the formulas given above for various CFEG STEMs that Nion has worked with. The first three columns show data for VG STEMs before correction. These uncorrected instruments were clearly much more limited by spherical rather than chromatic aberration. The analytical VG HB501 was able to put a current of 0.3 nA into a probe just smaller than 0.5 nm. The "high-resolution" VG HB501 improved on this slightly and could reach a probe size of 0.21 nm at a much reduced beam current. The high-resolution VG HB603 improved on both these figures, with a probe size of 0.12 nm at a small beam current, and an ability to deliver 0.3 nA of current into a 0.22 nm probe.

With a C_3-only aberration corrector and doubled gun brightness, the theoretical performance of the VG HB501 improved significantly: the smallest probe size became 84 pm at 100 keV, and the probe sizes for a current of 0.3 and 1 nA became 122 and 184 pm, respectively. The corrected VG HB603 improved by a similar margin, to a 51 pm small-current probe, and a 0.3 nA, 90 pm probe. Because of the small energy spread of their CFEG guns and relatively small values of C_c, both these instruments were still limited more by geometric than by chromatic aberrations.

The C_3/C_5 corrector of the Nion UltraSTEM changed the situation. The geometric aberrations are now corrected so well that the chromatic aberration becomes more limiting. With the UltraSTEM column mounted on top of the VG 100 keV gun, the theoretical performance for small currents is worse than the corrected VG 603 (66 pm probe vs. 51 pm for the 300 keV instrument), but it improves at larger beam currents—the UltraSTEM is

TABLE II Theoretical Probe-Forming Performance of Various CFEG STEMs

	VG 501 analysis	VG 501 high resolution	VG 603 high resolution	Corrected VG 501	Corrected VG 603	UltraSTEM 100	UltraSTEM 200
E_o (keV)	100	100	300	100	300	100	200
λ(pm)	3.70	3.70	1.97	3.70	1.97	3.70	2.51
Limiting geometric aberration	$C_{3,0}$	$C_{3,0}$	$C_{3,0}$	$C_{5,4}$	$C_{5,4}$	$C_{7,8}$	$C_{7,8}$
Aberration value (mm)	3.5	1.3	1.0	60	60	20	20
Geometric resolution limit (pm)	***260***	***203***	***118***	***83***	***49***	37	26
C_c (mm)	3.5	1.3	1.5	1.4	1.7	1.3	1.5
δE (eV)	0.35	0.35	0.35	0.35	0.35	0.35	0.35
Chromatic resolution limit (pm)	106	65	29	67	31	***65***	***41***
Aberration-limited resolution (pm)	**260**	**203**	**118**	**83**	**49**	**65**	**41**
Optimum aperture semi-angle (mr)	8.7	11.1	10.2	27.3	24.6	34.8	37.7
Brightness (A/(m^2 sr))	1×10^{13}	1×10^{13}	4×10^{13}	2×10^{13}	4×10^{13}	2×10^{13}	4×10^{13}
Probe size for 10 pA (pm)	**270**	**211**	**123**	**84**	**51**	**66**	**41**
Probe size for 100 pA (pm)	**348**	**272**	**158**	**98**	**65**	**77**	**48**
Probe size for 300 pA (pm)	**478**	**373**	**218**	**122**	**90**	**96**	**60**
Probe size for 1 nA (pm)	**777**	**606**	**354**	**184**	**146**	**145**	**90**

The resolution limit that determines the aberration-limited performance of each microscope is shown in ***bold italics***.

able to pack 0.3 nA beam current into a 96 pm probe, and 1 nA into a 145 pm probe. Mounted on top of a 200 keV CFEG source that we are building and testing, the UltraSTEM is expected to have a small-current probe of 41 pm and deliver 1 nA into a 90 pm probe.

With the exception of the Nion 200-keV STEM, which remains to be thoroughly tested, most of the cited numbers are closely borne out in practice. This includes the large-current performance of the UltraSTEM 100, which has proved itself able to put 0.3 nA current into a probe of ~100 pm, and 0.7 nA into a probe of ~130 pm (Muller *et al.*, 2008).

When estimating probe sizes for currents > 1 nA, the gun aberrations typically need to be taken into account, and this has not been done here. However, a corrector can correct aberrations originating in the gun just as easily as those originating in the objective lens, so the influence of the gun aberrations will be much less than in pre–aberration-correction days. Note also that when a large d_{source} is being used, the illumination half-angle can be opened up slightly relative to the low-current optimum without a significant additional deterioration in resolution. This strategy is especially useful when the optics is limited by chromatic aberration, since in this case the aberration-limited probe size increases only linearly with the illumination angle. It was, for instance, used by Muller *et al*. (2008).

It would be interesting to estimate the performance of other STEMs using the above formulas, particularly STEMs with Schottky guns. However, because the published range of Schottky brightness and energy spread values is rather broad and we have not measured the values ourselves, it is not possible for us to assess these instruments accurately. Using Müller *et al.'s* (2006) values ($B_r = 2.1 \times 10^7$ A/(m^2 sr V), energy spread $\delta E = 0.7$ eV and $C_c = 2.4$ mm), the above formulas indicate that the corresponding instrument is likely to be limited by chromatic aberration and that it should be able to reach a probe size of just over 50 pm at 300 keV for small beam currents. The probe size, however, will increase rapidly at larger beam currents, to over 0.3 nm at 1 nA. At 100 keV, the large-current (0.3 and 1 nA) probe sizes for such an instrument are likely to be similar to those of the uncorrected VG HB501.

B. Complications Resulting From Aberration Correction

Major gains often come with new complications, and this holds for aberration correction, too. One standard complication for aberration-corrrected STEM is that the available dark field signal becomes weaker for higher resolutions. As the angular range of the probe is increased to attain a smaller probe size, a progressively larger fraction of elastically scattered primary electrons remains within the BF cone and is thus not available for DF imaging. Moreover, the low-angle HAADF cutoff needs to increase in proportion to the increase in the angular range of the probe, otherwise the

HAADF images become progressively more nonlinear (Hartel, Rose, and Dinges, 1996). Detailed simulations of this effect for aberration-corrected probes remain to be performed, but it is clear that either the HAADF signal available from each atom will grow progressively weaker as the STEM resolution is improved (if the low-angle HAADF cutoff is increased), or the HAADF images will become more coherent and nonlinear, and therefore harder to interpret (if the lower angular limit is not changed). These effects will be particularly important for light atoms whose scattering is more forward-peaked.

The electrons that reach the DF detector are scattered from the deep and partially screened potential well surrounding the atomic nucleus (e.g., Kirkland, 1998). It is useful to note that the atomic scattering center is much smaller than the atomic size defined by the valence electrons, and that this causes the angular distribution for elastic scattering to extend to large angles. As a result, the HAADF resolution has been able to progress well below the separation of near-neighbor atoms in solids, and beyond the resolution of imaging techniques that probe the distribution of valence electrons, such as scanning tunneling microscopy (STM). Depending on the Z of the atom, the size of the scattering center is of the order of 10–30 pm. The HAADF image is further broadened by the thermal vibrations of the atomic nucleus, which have a root-mean-square magnitude $\sim$10 pm at room temperature (Loane, Xu, and Silcox 1991). Even so, atomic images less than 50 pm wide should ultimately become available. At probe sizes below 100 pm, however, the apparent size of the atomic scattering center needs to be explicitly taken into account in estimating the HAADF resolution, especially for lighter atoms such as carbon and oxygen. It even makes a significant contribution to the size of the images of heavy atoms such as gold (Batson, 2006).

Another readily foreseeable complication is that in a crystal, electron probes with the high convergence needed for sub-angstrom resolution spread onto neighboring atomic columns. This can be modeled by simulating the propagation of the probe through the crystal (Ishizuka, 2001; Dwyer and Etheridge, 2003; Peng, Nellist, and Pennycook, 2004; Allen *et al*., 2006). A very simple approximation is that spreading onto neighboring columns for highly convergent probes that are not strongly bound to individual atomic columns will occur for sample thicknesses greater than

$$t_{max} \sim d_{col}/(2\alpha) \sim d_{col}d_{res}/\lambda, \tag{18}$$

where d_{col} is the distance between the neighboring atomic columns and d_{res} the resolution corresponding to the probe half-angle α. For $d_{col} = 0.2\,\text{nm}$ and $d_{res} = 0.05\,\text{nm}$, Eq. (18) gives $t_{max} \sim 3\,\text{nm}$ for a 100 keV beam and $t_{max} \sim 4\,\text{nm}$ for a 200-keV beam. Focusing the probe so that it is the smallest in the center of the sample rather than at the entrance face can probably

double the thickness limits to 6 and 8 nm, respectively, but even the larger figures are smaller than the typical thickness of a crystalline sample of 10–30 nm. For an inter-columnar spacing of 0.2 nm in a 20 nm thick crystalline sample, the probe will start spreading onto neighboring columns at HAADF resolutions better than 100 λ. In aberration-corrected instruments the probe size is typically 20–50 λ, which means that probe spreading onto neighboring columns in samples of typical thickness is likely to be the norm in all advanced EMs. A detailed calculation of the probe propagation though the sample will then be needed to interpret both HAADF images and spectroscopic data.

The above effect is the "other side of the coin" of improved *z*-depth resolution, which can be used to assign atoms to different heights in a sample without needing to use a series of tilts (van Benthem *et al*., 2006; Borisevich *et al*., 2006). Such capabilities will become significantly enhanced as the resolution grows better, especially at lower primary energies (larger electron wavelengths).

IV. NEW APPLICATIONS

The improved performance of aberration-corrected instruments has produced many new applications for STEM imaging and analysis. Numerous examples are described in this volume. As instrument designers and makers, we admire the inventiveness of the users of the new instruments and the elegance of the results. At the same time, we need to look toward the future and concentrate development efforts on areas not yet fully explored. Presently we see three areas that hold exceptional promise. We describe them in the following subsections.

A. Atomic-Resolution Imaging and Analysis at Low Primary Energies

Even though the probe-forming capabilities of an aberration-corrected microscope will typically be better when operating at a higher primary energy than at a lower one, the optics improvements are now such that even low-energy operation can provide atomic resolution (Dellby *et al*., 2008). Low energies have several advantages: increased cross-sections for elastic and inelastic scattering and thus a higher signal from each atom, decreased radiation damage due to the knock-on mechanism, and slightly better localization of inelastic scattering and thus potentially higher resolution in elemental maps [see Eq. (19) below].

Figure 3 shows a HAADF image of <110> Si acquired at 60 keV with the Nion UltraSTEM100. The Si dumbbells that are separated by 0.136 nm are resolved. Figure 4 shows HAADF and STEM BF images of a carbon

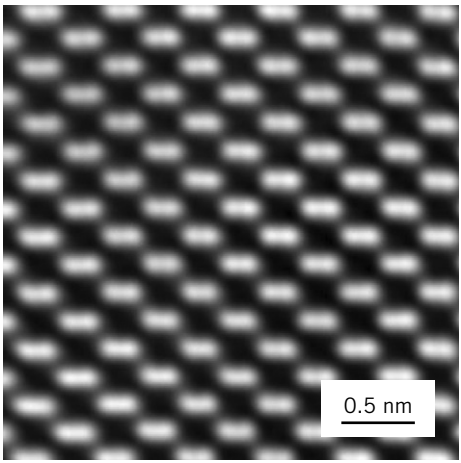

FIGURE 3 < 110 > Si STEM HAADF image recorded at 60 keV primary energy, Fourier-filtered to remove statistical noise. Nion UltraSTEM, 0.1 nA probe.

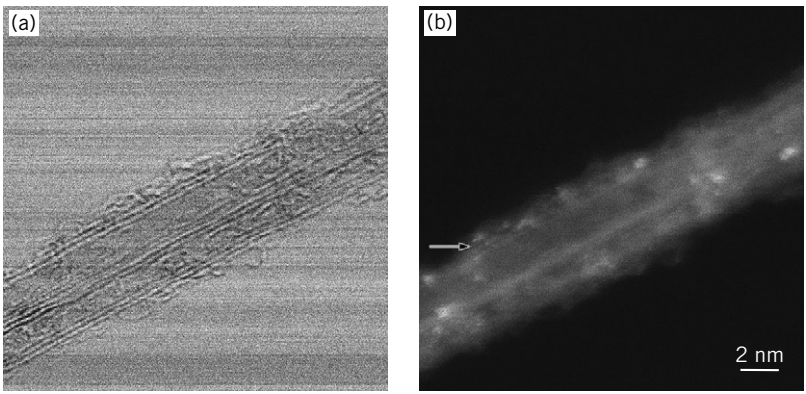

FIGURE 4 Bright-field (a) and HAADF (b) images of a carbon nanotube obtained at 60 keV primary energy. (Sample courtesy Dr. Mathieu Kociak.)

nanotube also acquired at 60 keV. Operating at this primary energy avoids radiation damage by knock-on displacement in materials such as boron nitride nanotubes, in which the knock-on threshold energy is 74 keV (Zobelli *et al*., 2007) and in carbon nanotubes, for which the theoretical knock-on threshold energy is 86 keV (Smith and Luzzi, 2001), but in which the intense electron beam of a STEM in fact produces weak but observable damage at 80 keV (Kociak, 2007).

The resolution at low primary energies is limited much more by chromatic aberrations than by geometric ones. Correction of the chromatic aberration would remove this limit. Unfortunately, simple combined

correctors of spherical and chromatic aberration (Zach and Haider, 1995a, 1995b) produce fifth-order aberrations of the order of several centimeters. Correctors that combine third-order, fifth-order, and chromatic correction (Rose, 2004; Haider *et al.*, 2008) are rather complicated even by aberration correction standards, and it remains to be seen whether they can be made to operate on a routine basis. Decreasing the energy spread of the electron beam to ~0.1 eV by an electron monochromator (Tiemeijer, 1999) can also improve the spatial resolution, especially if the loss of brightness is minimized by using a zero-final-dispersion design (Rose, 1990b; Kahl and Rose, 2000; Martinez and Tsuno, 2004). The monochromation approach also has the advantage that the energy resolution of electron energy-loss spectroscopy (EELS) is improved, thereby providing new information about the sample (Kimoto *et al.*, 2005; Lazar *et al.*, 2006, Browning *et al.*, 2006). This is the approach we plan to adopt in the future.

Applying the resolution relations of the previous section to the Nion C_3/C_5-corrected CFEG STEM shows that even without monochromation, this column is capable of atomic resolution ($d < 150$ pm) at 40 keV. Producing atom-sized electron probes at primary energies ~10 keV will only be possible using one of the approaches outlined above.

B. Atomic-Resolution Spectroscopy and Elemental/Chemical Mapping

Elemental mapping in the EM can potentially use emitted X-rays, emitted Auger electrons, or transmitted electrons which have lost energy as the collected signal. Because the initial excitation resulting from an energy loss event is usually more likely to decay by the emission of an Auger electron than of an X-ray (e.g., Reimer, 1997), the characteristic cross-sections for X-ray emission are typically much smaller than those for energy loss. The signal collection is also typically less efficient for the X-rays, at ~1–3% vs. > 50% for the EELS. These factors generally lead to more favorable signal-to-noise ratios (SNRs) for the EELS signal than for the X-ray signal, especially for low-Z elements (Leapman and Hunt, 1991; Leapman, 2004). The Auger signal has a limited escape depth and is not suitable for subsurface analysis. This makes the EELS signal the most promising one for elemental mapping at atomic resolution.

Three main requirements must be met if elemental mapping with atomic resolution by EELS is to be reached:

1. the instrumental resolution (i.e., the probe size in the STEM) must be sufficiently small,
2. the selected EELS signal must be sufficiently localized on the atomic columns of interest, and

3. the signal strength and collection efficiency must be such that a sufficiently large SNR is reached before radiation damage or instrumental drift invalidate the experiment.

The first requirement has been discussed extensively above. The second requirement accounts for the delocalization of inelastic scattering, i.e., for the fact that an electron passing some distance from an atom can still ionize it, and that the effective interaction region can therefore be much larger than the atom itself. A simple formula describing the delocalization that is in good agreement with experimental evidence was given by Egerton (1996)

$$d_d = 0.5\lambda/{\theta_E}^{3/4}, \tag{19}$$

where d_d is the diameter encompassing 50% of the inelastic interactions, θ_E the characteristic angle for inelastic scattering given by $\theta_E = \Delta E/2E_o^*$, ΔE the energy loss, and E_o^* is the "relativistically corrected" primary energy E_o. For an energy loss of 500 eV, Eq. (19) predicts $d_d = 0.18$ nm at 100 keV and 0.24 nm at 300 keV primary energy. In reality, the situation is more complicated, and the localization of the detected inelastic signal can be enhanced significantly by opening up the collection angle (Muller and Silcox, 1995), especially if low-angle inelastic scattering is excluded by using an annular aperture in front of the EELS (Rafferty and Pennycook, 1999). With wide collection angles, it can also be improved by using energy losses higher than the edge threshold, that is, by enhancing the contribution of the electrons scattered into the Bethe ridge. These enhancements, however, come at the cost of a diminished signal, and it therefore remains to be confirmed by experiment whether they will be of practical use.

The third requirement arises because a feature is only identifiable if its SNR exceeds a lower limit, usually taken to be 3. Because of the weak signals involved, such a limit may not always be reached. The cross-sections of the characteristic inner-shell loss edges used for analysis are typically in the range of 10^{-8} to 10^{-5} nm^2 i.e., 10^2 to 10^5 times weaker than cross-sections for elastic scattering (Egerton, 1996), and they appear on a continuous background that must be subtracted sufficiently accurately. To make the SNRs of EELS maps approach the SNRs available in HAADF images, $\sim 10^3$ times stronger incident dose is needed per pixel for mapping a pure element, and a higher dose still is needed for mapping a minority element in a matrix. At the same time, the collection efficiency for the EELS signal needs to approach 100%.

Two instrumental solutions exist for EELS elemental mapping: energy-filtered TEM (EFTEM) using an energy filter acting on a broad-beam image (e.g., Reimer, 1995; Grogger *et al*., 2005), and the STEM approach of collecting an EEL spectrum at every pixel in the scanned image (Jeanguillaume and Colliex, 1989; Tencé, Quatuccio, and Colliex, 1995).

EFTEM is capable of collecting data in parallel from image areas of up to the size of its two-dimensional (2D) detector (typically a CCD with 1k × 1k or 2k × 2k pixels, but often binned down to 512 × 512). The large field of view and the fact that only a few energy-selected images are needed to produce a map of each element in the sample make EFTEM fast and convenient. Compositional maps of many elements can be acquired in a few seconds or tens of seconds, at ~0.4–2 nm resolution, provided that the studied area is illuminated with an incident beam current of the order of 10–100 nA (Krivanek, Kundmann, and Kimoto, 1995; Freitag and Mader, 1999; Grogger *et al.*, 2005). However, when attempting to reach atomic resolution (better than 0.2 nm) in elemental maps, EFTEM runs into problems with all three requirements listed above.

The EFTEM image is formed by the microscope's post-sample optics, whose aberrations therefore act on an electron beam that is considerably spread both in angle and energy by scattering from the sample. The chromatic resolution limit is especially severe for wide energy windows (> 10 eV). Avoiding much-worsened resolution resulting from electron-optical limits thus demands that both the energy width and the range of scattering angles admitted through the objective aperture be restricted. This reduces the collection efficiency and typically worsens the SNR. Moreover, restricting the range of angles accepted into the energy-selected image eliminates the high-angle energy-loss signal, which contains the high spatial resolution information about the sample. This limits the resolution attainable with small acceptance angles even more than the unavoidable diffraction limit due to the aperture. Finally, EFTEM data along the energy axis must be acquired serially—a separate exposure must be made for each new energy point. Energy-loss electrons not admitted into the energy-filtered image are simply lost. This lowers the SNR per given illumination dose level relative to more efficient acquisition methods. Correction of the aberrations of the imaging column, in particular of its chromatic aberration, would make the EFTEM instrumental resolution limitation less severe. But even when chromatic aberration correction does become available, the overall efficiency of the EFTEM technique will still be limited by the serial nature of the acquisition of information along the energy axis.

Another limitation for the EFTEM approach arises in the quantification of minority or trace elements, which needs many data points along the energy axis if the weak signal is to be extracted as reliably as possible. Acquiring the energy data serially is then especially inefficient. Because the doses required for elemental mapping at atomic resolution are much higher than those for imaging with elastically scattered electrons, the increased dose and hence larger radiation damage due to the EFTEM approach is likely to be a major concern.

The STEM/EELS spectrum-imaging approach is better suited to all the three principal requirements for atomic-resolution elemental mapping. The

instrumental resolution is determined by the pre-sample optics, which acts on a beam that has not been spread in angle and energy by the sample. With optimized collection optics, it is possible to accept electrons scattered by 50 mr or more into the energy loss spectrometer. Such relatively large angles improve both the localization of the signal and the collection efficiency. A full spectrum is available at each pixel, making it possible to use techniques such as principal component analysis (e.g., Trebbia and Bonnet, 1990; Bonnet, Herbin, and Vautrot, 1997; Stone, 2004; Bosman *et al*., 2006) and multiple least squares fitting (e.g., Leapman, 2004) to optimally extract weak signals in the presence of statistical noise.

The STEM approach is prone to one major limitation: speed. Acquiring a complete EEL spectrum with sufficient SNR with an incident beam current of 10–100 pA and EELS collection optics of ∼10–30% efficiency (as was the case prior to aberration correction and optimized collection optics) requires an acquisition time of ∼0.1–1 s per pixel. An elemental map of 256 × 256 pixels acquired and processed at 0.1 s per pixel takes 1.8 hours, which is beyond the patience of most operators.

If the acquisition time could be reduced, then the intrinsic advantages of STEM spectrum-imaging would become very clear. Speeding up the acquisition to 1 ms per pixel would reduce the total acquisition time to a much more acceptable 66 s per 256 × 256 map. An improvement factor of 100× is not impossible: a 33× improvement in the incident current plus a 3× improvement in the EELS collection efficiency would reach it. This amounts to increasing the probe current to ∼1 nA while maintaining its size close to 0.1 nm and improving the collection efficiency to nearly 100%.

As the instrumental performance has been approaching such levels, interest in atomic-resolution STEM-EELS mapping has grown correspondingly. Several groups have demonstrated the potential of the technique: Bosman *et al*. (2007) on a sample of $Bi_{0.5}Sr_{0.5}MnO_3$; Kimoto *et al*. (2007) and Kimoto, Ishizuka, and Matsui (2008) on $La_{1.2}Sr_{1.8}Mn_2O_7$, and Si_3N_4; Watanabe *et al*. (2007) on $SrTiO_3$, and Muller *et al*. (2008) on a $La_{0.7}Sr_{0.3}MnO_3/SrTiO_3$ multilayer sample. The acquisition conditions have varied widely. Kimoto *et al*. (2007) used a 200-keV CFEG STEM that did not have an aberration corrector and produced only a 7 pA current in a 0.12 nm probe. Their collection semi-angle was 31 mr, and the acquisition time 2 s per pixel. Drift was compensated by recording and re-registering a small HADF image close to the area of interest, once every 30 s, and the total acquisition time for a 24 × 61 pixel map was 61 minutes. Bosman *et al*. and Watanabe *et al*. used C_3-corrected STEMs with more probe current, probably of the order of 100–200 pA, less optimized EELS collection optics (acceptance angles of the order of 15–25 mr), and acquisition times of 0.1–0.2 s per pixel. Muller *et al*. used a C_3/C_5-corrected CFEG STEM with 780 pA current in a 0.14 nm probe with a 40 mr convergence angle and a 45 mr collection angle. The acquisition time was only 7 ms per pixel, no drift

correction was performed, and a 64 × 64 pixel map needed just 29 s net acquisition time. The SNR of Muller *et al*.'s spectra was good enough for probing bonding variations across the sample. The La, Mn and Ti elemental maps obtained by Muller *et al*. are shown in Figure 5 together with a red-green-blue composite image combining the three elemental maps.

Table II shows that 1 nA current is presently available in probes ~0.15 nm in diameter, and that 0.1 nm probes containing 1 nA of current should be available soon. With present CFEG designs, the probe current can probably be increased 2× to 5× higher still while maintaining atomic resolution before gun aberrations decisively limit further increases. At the

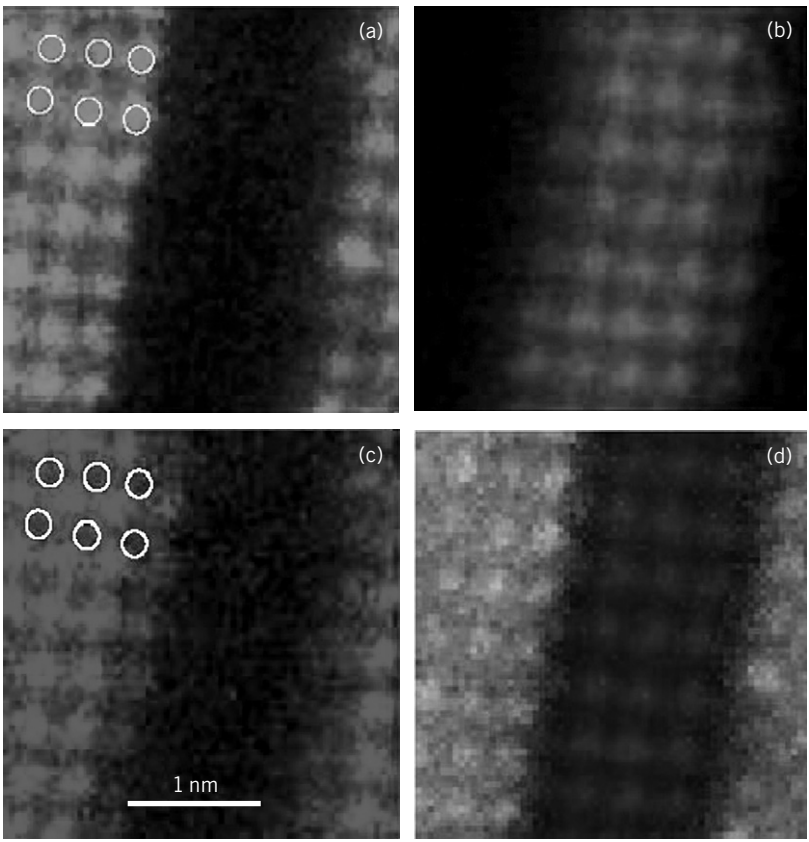

FIGURE 5 Color-coded elemental maps of a $La_{0.7}Sr_{0.3}MnO_3/SrTiO_3$ multilayer. (a) La; (b) Ti; (c) Mn; and (d) RGB representation of the sample obtained by combining the individual maps. Note how Ti and Mn occupy the same type of sites in the lattice, and that the purple dots at multilayer boundaries indicate intermixing of Ti and Mn within each column. (Courtesy Lena Fitting-Kourkoutis and David A. Muller, with permission from *Science*.) (See color insert).

increased current, atomic-resolution elemental mapping should be possible with per-pixel acquisition times of the order of 1 ms. With readout rates >1 MHz for the EELS CCD detector, which are now standard, it should be readily possible to record the intensity in 1000 energy channels per pixel at this pixel advance rate. No present-day EEL spectrometer is capable of such overall speed yet, but the limitation is likely to be overcome within the next few years. When this state of development is reached, atomic-resolution EELS maps of 256×256 pixels should be obtainable in just over 1 minute.

An attendant complication for achieving atomic resolution in elemental maps is likely to be that the channeling of the probe down the atomic columns will have to be simulated to ensure that the initially sharply focused probe does not spread excessively in thicker samples when high probe angles are used. Radiation damage will have to be monitored carefully, and the beam will have to be blanked whenever no data are being acquired. Even with these factors, it would be surprising if the ability to map the composition of solid samples at atomic resolution on a time scale of one to a few minutes did not find widespread use.

C. Single Atom Spectroscopy and Mapping

The requirements for single-atom spectroscopy are slightly different from atomic-resolution mapping. Resolution of 0.2 nm or better will help to optimize the detection limits, but it is not an absolute requirement—atoms with poorly localized low-energy edges may be detectable even though their EELS images may be >0.5 nm wide. On the other hand, the SNR of the EELS signal collected from the single atom is paramount. In order to identify a single atom unequivocally, the SNR resulting from the atom should ideally be much greater than the simple detection threshold of $\mathrm{SNR} = 3$ (Krivanek *et al*., 1991).

In a pioneering study of the detection limits by EELS, Isaacson and Johnson (1975) predicted that a single atom of fluorine in a 2 nm thick carbon matrix should be detectable in a per-pixel dwell time of 0.01 s with an electron probe of 1 nA current and 0.3 nm diameter and a 100% efficient parallel-detection EELS. Probes of comparable and greater energy density and efficient EEL spectrometers are now available, and it is therefore not surprising that single atoms are being detected spectroscopically and mapped.

Suenaga *et al*. (2000) used an uncorrected analytical VG with a 0.6 nm, 0.65 nA probe at 100 keV, an illumination half-angle of 8 mr, and probably a similar detection half-angle. They formed EELS spectrum-images of single Gd atoms encapsulated in fullerene spheres that were stuffed inside a single-wall carbon nanotube, using the gadolinium $N_{4,5}$ edge with 140-eV threshold energy and a high cross-section but moderate localization of

~0.4 nm. The Gd atoms were spaced by 1–3 nm. A spectrum-image 128 × 32 pixels in size was recorded at 35 ms per pixel (i.e., a net acquisition time of 145 s). Quantifying the spectrum-image into an elemental map produced an SNR just high enough to identify single Gd atoms. A CCD detector, for which detective quantum efficiency (DQE) ~1 for a wide range of operating conditions (Krivanek and Mooney, 1993; Hunt *et al.*, 2001; Tencé *et al.*, 2006), was used, but the probe characteristics could have been much better optimized if an aberration-corrected STEM were available. As a result, the SNR for the Gd $M_{4,5}$ edge at 1217 eV, whose cross-section (per 1-eV energy interval) is ~100× weaker than the $N_{4,5}$ cross-section, was far from sufficient, and this edge could not be used. Radiation damage was severe enough at 100 keV that many of the Gd atoms left their fullerene cages. Even so, a clear elemental map showing single Gd atoms was obtained.

It would be very interesting to repeat this experiment at lower primary energy, with aberration-corrected probe-forming optics, and an optimized EELS collection and detection setup to determine whether the radiation damage could be minimized, and whether electronic and magnetic information about single atoms of Gd might become available with a sufficiently strong Gd $M_{4,5}$ signal.

The detection of single atoms of Ca in a biological sample has been demonstrated by Leapman (2003). The sample consisted of isolated Ca atoms and Ca aggregates on a carbon film just 4 nm thick. An uncorrected analytical VG was used at 100 keV, with a probe of ~1 nm in diameter and 1 nA current. The EELS collection half-angle was 20 mr, and the sample was held at −160°C. The per-pixel dwell time was 0.1–0.4 s, the energy dispersion 0.3 eV per channel, and the pixel size typically 0.6 × 0.6 nm. SNR of 5 for single Ca atom detection was obtained. Similar methodology applied to atoms of iron on the same type of substrate yielded an SNR ~10 for detecting a cluster of four Fe atoms–not quite high enough for single-atom detection.

An experiment by Varela *et al*. (2004) on isolated La atoms substituting for Ca in $CaTiO_3$ points to the possibilities opened by aberration correction (Figure 6). Spectra were collected from a Ca column containing a lanthanum atom (spectrum b, for which the bright spot in the HAADF image is more intense than at neighboring Ca-only columns), and from various points in the vicinity (spectra a, c, and d). The EELS SNR was sufficient to detect the La atom using its $M_{4,5}$ edge at 832-eV energy loss. A weak La $M_{4,5}$ signal was still detectable when the probe was centered on neighboring O and Ti-O columns (0.2 and 0.28 nm distant, respectively), but not when the probe was centered on a neighboring Ca-only column (0.4 nm distant). Simulation of the probe propagation through the sample showed that the signal was due to probe dechanneling rather than the delocalization of the inelastic scattering. A C_3-corrected VG HB501 with an

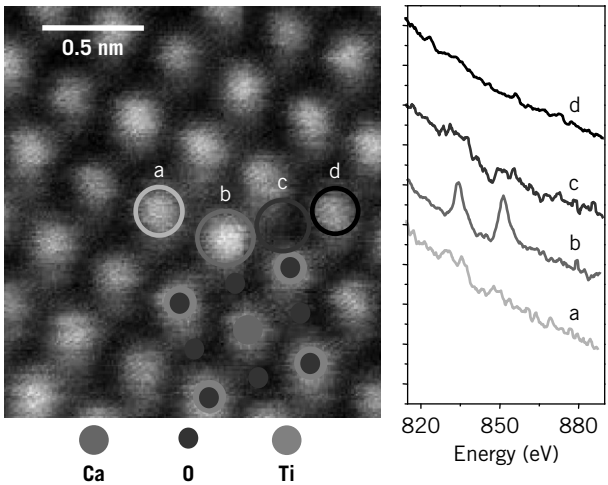

FIGURE 6 HAADF image of $CaTiO_3$ sample with a La atom impurity, and EELS spectra recorded in 20–30 seconds from various points on and near the La atom. (Courtesy Maria Varela and Stephen J. Pennycook, with permission from *Physical Review Letters*.) (See color insert).

energy loss spectrometer equipped with a 2D CCD detector was used at 100 keV, with an illumination half-angle of 25 mr, a probe current of 100 pA in a 0.11 nm probe, and a collection half-angle of 7 mr. The nonoptimized EELS collection geometry meant that less than 8% of the available EELS signal was collected. This was partially compensated by a long total acquisition time: 30 s for the spectrum collected over the La atom and 20–30 s each for the other spectra.

In order to understand the relative importance of the different factors contributing to the quality of the collected spectra, it is useful to derive the SNR that should have been reached in the above experiment. Neglecting multiple scattering, the signal from the atom of interest is given approximately by

$$S_a = I_p \sigma_a \varepsilon_a t / \left(\left(d_p^2 + d_d^2 \right) e \right), \tag{20}$$

(Leapman, 2003), where I_p is the probe current, σ_a the cross-section for the atom's monitored signal, ε_a the detection efficiency for the atom's signal, t the acquisition time, d_p the probe size, d_d the delocalization of the inelastic scattering [given by Eq. (19)], and e the charge carried by an electron. $(d_p^2 + d_d^2)^{0.5}$ may be taken as an "effective probe size" due to the combined influence of the probe-forming optics and the scattering delocalization.

The background under the signal S_a is given by

$$S_b = I_p \sigma_b \rho_b \varepsilon_b t/e, \tag{21}$$

where σ_b is the average cross-section for the matrix atoms' contribution to the background, ρ_b the number of atoms per unit area of the sample, and ε_b the detection efficiency for the background signal (which may differ from ε_a if the angular distributions of the two signals are different).

Assuming that the dominant noise term is the statistical variation in the background signal, and that the efficiencies ε_a and ε_b are both equal to ε, the SNR of the single atom's signal is then

$$\text{SNR} = S_a/\sqrt{S_b} = \left[\sigma_a/\left(d_p^2 + d_d^2\right)\right]\left[I_p \varepsilon t/\left(\sigma_b \rho_b e\right)\right]^{0.5}. \tag{22}$$

Equation (22) shows that maximizing the signal cross-section σ_a improves the SNR linearly, whereas increasing the probe current, collection efficiency, or acquisition time or decreasing the background cross-section or atomic density per unit area (by decreasing the sample thickness) only improve it as the square root. Decreasing the probe diameter improves the SNR as $1/d_p^2$ when $d_p >> d_d$, as $\sim 1/d_p$ when $d_p \sim d_d$, and does not change the SNR at all when $d_p << d_d$.

Note that when the probe size d_p is made smaller, decreasing the probe current or the acquisition time as $(d_p^2 + d_d^2)^2$ keeps the SNR at each pixel unchanged. As the resolution improves, the pixels need to become more closely spaced, but even so the required dose per unit area decreases as $(d_p^2 + d_d^2)$. This means that decreasing the probe size by using aberration-corrected electron optics provides the same SNRs for detecting individual atoms at *smaller* incident doses per unit area. The improvement is a major one: decreasing the effective probe size from 1 nm to 0.2 nm decreases the required dose per unit area 25×, even though the spatial resolution in the elemental map will now be 5× better.

It is also worth noting that when the electron probe size is ∼0.1 nm in diameter and yet intense enough to produce high-quality EELS data, and the delocalization is not much larger than 0.1 nm, detecting minority and trace elements in normal samples becomes possible on an atom-by-atom basis. The concentrations corresponding to a single atom in a probed volume in a sample 5–30 nm thick are 1–10% when the delocalization is better than 0.1 nm, and 0.1–1 % when the delocalization is 0.3–0.5 nm. In other words, because the atoms are probed one at a time, even trace atoms present in real concentrations << 0.1 % should be detectable.

Applying Eq. (22) to the La detection experiment, we used experimental cross-sections derived from the EELS atlas data (Ahn and Krivanek, 1993) as much as possible. To do this, we first calculated the Hartree-Slater

cross-section for the La $M_{4,5}$ edge continuum (3.3×10^{-7} nm^2 for an energy interval 50-eV wide starting 30 eV past the threshold), then scaled the experimental $M_{4,5}$ white line intensities and pre-edge background to the edge continuum using the La_2O_3 data in the atlas. We estimated the contribution of the adjacent columns in the $CaTiO_3$ sample by using the measurements of Varela *et al*. (2005) of how much La signal was recorded when the probe was positioned over the neighboring atomic columns. Taking the sample thickness to be ~20 nm then meant that when the probe was centered on the Ca column containing the substitutional La atom, the contributions to the spectrum came from an effective total of 125 atoms (some of which were located on neighboring columns illuminated by the dechanneled probe), with the relative proportions La 0.8, Ca 38.2, O 46, and Ti 15. We also accounted for the pre-edge background being weaker in this type of sample than in La_2O_3 by scaling the edge background cross-section by a ratio determined by computing theoretical spectra appropriate to the mostly Ca-Ti-O sample under the probe in the present experiment and to the atlas sample (La_2O_3). Assuming that the DQE of the CCD detector was close to 1 then gave a net signal strength of 5.2×10^3 electrons in the La M_5 threshold peak that was recorded as ~3 eV wide in the experiment, and a background height of 1.5×10^4 electrons per 1-eV wide channel just in front of the La edge. This led to SNR of 22 for the total M_5 threshold peak intensity from the single La atom relative to the statistical noise of the background signal under the peak. Assuming that the detector point spread function was 1 eV wide then gave a ratio of the M_5 net peak height to the peak-to-peak noise in the background of 4.3:1. Both these numbers are in good agreement with the experiment, showing that our understanding of the principal factors determining the strength of the recorded signal and of its background is sound. The numbers also show why the acquisition time had to be 30 s long: the La $M_{4,5}$ edge would not have been readily visible in a spectrum acquired in a second or less.

We also estimated the La white line SNR using the EELS Advisor simulation software package (Gatan Inc., Pleasanton, CA) developed recently (Menon and Krivanek, 2002; Menon, 2005; Hunt and Menon, 2005). Unfortunately, we found that the present version of the software does not properly account for collection efficiency when the collection aperture is smaller than the illumination aperture (as was the case in the present experiment), does not model threshold white lines and background intensities with sufficient accuracy, and further underestimates the shot noise contribution to spectra. Nevertheless, we found that the errors approximately canceled out and that a reasonable agreement with the above SNR estimate as well as with the experimental data was obtained.

In future La imaging experiments in an optimized instrument, the probe current will probably be ~10× higher and the collection efficiency also ~10× higher. The same SNR for identifying a single atom as was attained

by Varela *et al*. will thus be obtainable in ∼0.3 s. Using optimized signal-extraction techniques such as principal component analysis should make it possible to reduce the per-pixel dwell time to ∼0.01 s, at which point a 256 × 256 pixel map optimized for La single-atom detection would take 11 minutes to acquire. With similar or better SNR than the one obtained in the experiment described above, it should also be possible to use the details of the white line intensity and shape to map the valence state and other properties of the single atoms.

La is a heavy atom, and detecting it in an EELS spectrum image is easier because it can be identified in a HAADF image before any spectra are taken. Reliable EELS imaging of single atoms that are similar to their matrix and therefore cannot be identified by HAADF imaging, as was done by Leapman (2003) for Ca in a very thin carbon sample, is more challenging. Figure 7 explores this situation with EELS spectra computed using the EELS Advisor, with a 100 keV, 0.15 nm diameter probe with 1 nA current, a collection semi-angle of 30 mr, and a DQE = 1 for the EELS detector. The visibility of EELS edges from single atoms is explored by simulating spectra recorded with the probe positioned over a single impurity atom for situations likely to be encountered on samples of practical interest. In a complete mapping experiment, spectra from other pixels near the single atom's center will also contain the atom's signature, and the SNR requirement for each contributing spectrum will therefore not be as strict as for a single spectrum.

The left column in Figure 7 explores detecting phosphorus in a carbon matrix, a situation that may arise in biological samples. The P $L_{2,3}$ edge lies in front of the strong carbon K-edge and is easily visible in a raw spectrum recorded in 0.01 s when the phosphorus is present in 1 at. % concentration (spectrum a). Because the P $L_{2,3}$ delocalization is ∼ 0.4 nm at 100 keV primary energy, the $L_{2,3}$ signal will be ∼10× weaker than if the delocalization had only been 0.1 nm. The middle spectrum (b) therefore simulates the strength of the signal when P is present in the probed volume at only 0.1 at. %. (Carbon density is ∼140 atoms/nm^3, and 0.1 at. % concentration therefore corresponds to 1 P atom in a probed volume 0.5 nm in diameter in a 36 nm thick sample.) The P $L_{2,3}$ edge then becomes essentially invisible in the unprocessed spectrum. However, calculating a simple difference spectrum, which can be readily obtained in a spectrum-imaging experiment by subtracting a properly scaled version of the average spectrum from the carbon matrix at places free of phosphorus atoms, still shows a strong P signal, provided that the acquisition time per pixel is lengthened to 0.1 s. Shortening the time to 0.01 s decreases the edge SNR 3×, but the signal is still unmistakable (spectrum c). We therefore conclude that rapid EELS mapping of isolated P atoms in a carbon matrix should be possible with presently available instrumentation, provided that radiation damage is avoided (for instance, by decreasing the primary energy to 60 keV).

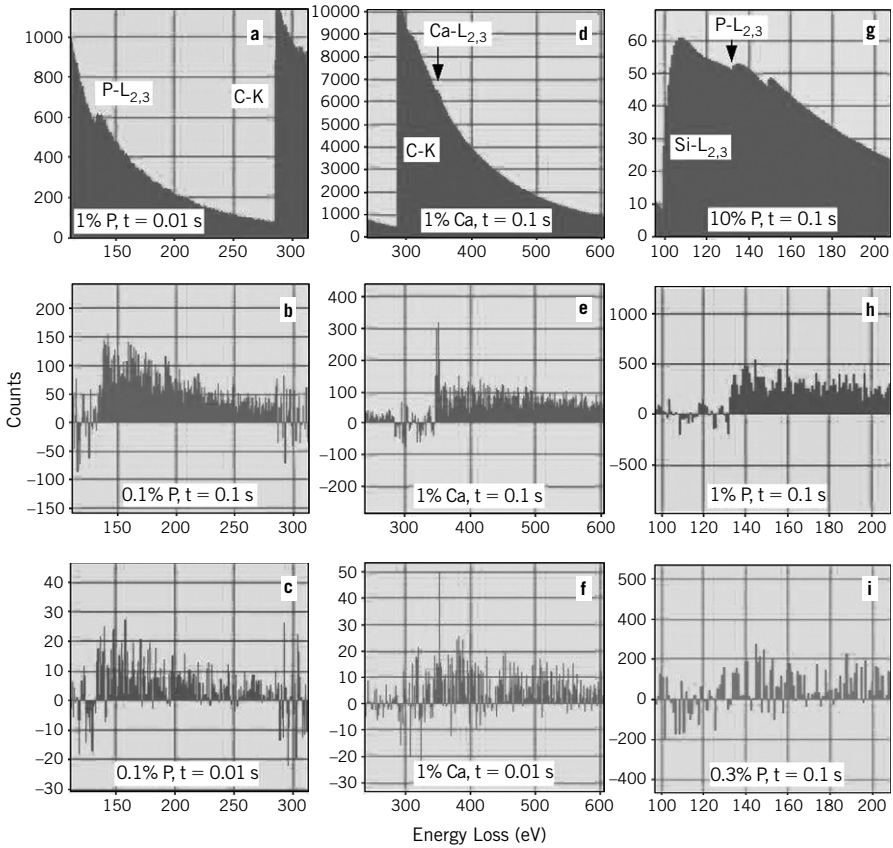

FIGURE 7 Simulated EELS spectra. Left column: phosphorus in C. Middle column: calcium in C. Right column: phosphorus in Si. 100 keV, 1 nA probe current, 0.15 nm probe diameter, 30 mr collection semi-angle (see text for detailed discussion).

The middle column in Figure 7 simulates a less favorable case, also with biological significance: Ca detection in a carbon matrix. The beam parameters are unchanged, but we are now dealing with the Ca $L_{2,3}$ edge riding on top of the dominant matrix edge. Better localization of the inelastic scattering ($d_d = 0.22$ nm at 100 keV) helps to prevent the spreading of the Ca signal due to delocalization, and the visibility of the Ca edge is aided by its strong threshold lines. Even so, the Ca edge is barely visible in an unprocessed spectrum recorded in 0.1 s for 1 at. % Ca concentration (spectrum d). (1 at. % concentration corresponds to one Ca atom in a probed volume 0.3 nm in diameter in a 10 nm thick sample.) The difference spectrum, however, shows the edge clearly for 1% concentration recorded in 0.1 s (spectrum e), and the edge is still recognizable in a spectrum recorded in 0.01 s (spectrum f). This suggests that rapid mapping of single atoms of

Ca in a carbon matrix with single atom sensitivity should also be possible, provided that the sample is not much thicker than 10 nm.

Note that in the above case, we are essentially exploring how the experiment performed by Leapman (2003) will work in an aberration-corrected CFEG STEM. The finding that decreasing the size of a 1 nA probe to 0.15 nm will make it possible to see single Ca atoms reliably in thicker samples and with shorter spectrum acquisition time is not surprising.

The right column in Figure 7 deals with a still more difficult case for single-atom mapping: P in Si, an example of the type of problems relevant in the semiconductor industry. Here we are dealing with an edge with no major threshold lines, riding on top of a very strong matrix edge, and with poor delocalization. Concentration of 1 at. % produces no readily identifiable features in the raw spectrum, and we have therefore shown the unprocessed spectrum for 10% concentration (spectrum g). Concentration of 1% is readily detectable in a difference spectrum acquired in 0.1 s (spectrum h). Silicon's atomic density is 50 atoms/nm^3, and 1% concentration therefore corresponds to 1 atom of P in a probed volume 0.5 nm in diameter and 10 nm thick. For a more realistic 30 nm thick crystalline Si sample, we would be dealing with an effective concentration of 0.3 at. %. In the corresponding difference spectrum (spectrum i), the P edge is barely detectable, even though the acquisition time is again 0.1 s. The same SNR would be obtained for a concentration of 1% and 0.01 s acquisition time. This example may therefore be at the edge of the possibilities for fast elemental mapping with presently available instrumentation, especially if the sample thickness cannot be kept to 10 nm or less.

To summarize, chemical mapping with single-atom sensitivity performed in a reasonable time ($<$10 min for a 256 $\times$ 256 map) is possible with present-day instrumentation, but practical success will very much depend on the situation at hand. Provided that radiation damage does not make the experiment impossible, mapping with single-atom sensitivity should be possible for most cases where a strong edge from the element of interest is available in the range of $\sim$100–1000-eV energy losses, especially if the edge of interest is not located on top of a strong feature in the matrix spectrum.

V. CONCLUSIONS

Aberration correction has greatly improved the performance and the range of useful applications of STEMs. It is now possible to form atomic-resolution images and spectra at primary energies as low as 60 keV. Moreover, electron probes can be produced that are smaller than the typical atom and yet contain enough current for rapid EELS analysis with

sensitivity down to the single atom level. This is leading to a new range of applications for the STEM-EELS technique, which may well begin to rival the sensitivity of the atom probe.

ACKNOWLEDGMENTS

We are greatly indebted to many of our colleagues, especially to Phil Batson, Andrew Bleloch, Mick Brown, Matt Chisholm, Christian Colliex, David Muller, Pete Nellist, Steve Pennycook, and John Silcox, for their unsparing support of our efforts in STEM aberration correction.

REFERENCES

Ahn, C. C., and Krivanek, O. L. (1983). "EELS Atlas." Gatan Inc., Warrendale, PA. Available at www.gatan.com.

Allen, L. J., Findlay, S. D., Oxley, M. P., Witte, C., and Zaluzec, N. J. (2006). Modeling high-resolution electron microscopy based on core-loss spectroscopy. *Ultramicroscopy* **106**, 1001–1011.

Archard, G. D. (1955). Two new simplified systems for the correction of spherical aberration in electron lenses. *Proc. Roy Soc.* **B68**, 156–164.

Batson, P. E. (2006). Characterizing probe performance in the aberration corrected STEM. *Ultramicroscopy* **106**, 1104–1114.

Batson, P. E., Dellby, N., and Krivanek, O. L. (2002). Sub-ångstrom resolution using aberration corrected electron optics. *Nature* **418**, 617–620.

Beck, V. (1979). Hexapole spherical-aberration corrector. *Optik* **53**, 241–245.

Bertein, F. (1947). Un système correcteur en optique électronique, *C. R. Acad. Sci. Paris* **225**, 801–803.

Bonnet, N., Herbin, M., and Vautrot, P. (1997). Multivariate image analysis and segmentation microanalysis. *Scanning Microscopy* **11,** 1–21.

Borisevich, A. Y., Lupini, A. R., Travaglini, S., and Pennycook. S. J. (2006). Depth sectioning of aligned crystals with the aberration-corrected scanning transmission electron microscope. *J. Electr. Microsc.* **55**, 7–12.

Bosman, M., Keast, V. J., García-Muñoz, J. L., D'Alfonso, A. J., Findlay, S. D., and Allen, L. J. (2007). Two-dimensional mapping of chemical information at atomic resolution. *Phys. Rev. Lett.* **99**, 086102-1-086102-4.

Bosman, M., Watanabe, M., Alexander, D. T. L., and Keast, V. J. (2006). Mapping chemical and bonding information using multivariate analysis of electron energy-loss spectrum images. *Ultramicroscopy* **106**, 1024–1032.

Browning, N. D., Arslan, I., Erni, R., Idrobo, J. C., Ziegler, A., Bradley, J., Dai Z., Stach, E. A., and Bleloch, A. L. (2006). Monochromators and aberration correctors: taking EELS to new levels of energy and spatial resolution. *J. Phys. Conference Series* **26**, 59–64.

Chen, E., and Mu, C. (1990). New development in correction of spherical aberration of electromagnetic round lens. *In* "Proc. Int. Symp. Electron Microscopy" (K. Kuo and J. Yao, eds., World Scientific, Singapore), pp. 28–35.

Chisholm, M. F., Lupini, A. R., Pennycook, S. J., Ohkubo, I., Christen, H. M., Findley, S. D., Oxley, M. P., and Allen, L. J. (2004). Simultaneous Z-contrast and phase contrast imaging of oxygen in ceramic interfaces. *Microsc. Microanal.* **10** (Suppl S02), 256–257.

Crewe, A. V. (2004). Some Chicago Aberrations, *Microsc. Microanal.* **10**, 414–419.

Crewe, A. V., and Kopf, D. (1980). A sextupole system for the correction of spherical aberration. *Optik* **5**, 1–10.

Dellby, N., Krivanek, O. L., Nellist, P. D., Batson, P. E., and Lupini, A. R. (2001). Progress in aberration-corrected scanning transmission electron microscopy. *J. Electr. Microsc.* **50**, 177–185.

Dellby, N., Krivanek, O. L., and Murfitt, M. F. (2006). Optimized quadrupole-octupole C_3/C_5 corrector for STEM. *Proceedings of CPO-7 Seventh International Conference on Charged Particle Optics*, p. 97. Available at: http://www.mebs.co.uk/CPO7%20-%20Abstract%20Book.pdf; also *Nuclear Instruments and Methods* (2008), in press.

Dellby, N., Murfitt, M. F., Krivanek, O. L., Kociak, M., March, K., Tencé, M., and Colliex, C. (2008). Atomic-resolution STEM at 60 kV primary voltage. *Microsc. Microanal.* **14**, Supplement 2, 136–137.

Deltrap, J. H. M. (1964). Correction of spherical aberration with combined quadrupole-octopole units. *Proc. EUREM-3*, Prague, p. 45.

Dwyer, C., and Etheridge, J. (2003). Scattering of ångstrom-scale electron probes in silicon. *Ultramicroscopy* **96**, 343–360.

Egerton, R. F. (1996). "Electron Energy-Loss Spectroscopy in the Electron Microscope," second edition. Plenum Press, New York.

Freitag, B., and Mader, W. (1999). Element-specific imaging with high lateral resolution: an experimental study on layer structure. *J. Microsc.* **194**, 42–57.

Grogger, W., Varela, M., Ristau, R., Schaffer, B., Hofer, F., and Krishnan, K. M. (2005). Energy-filtering transmission electron microscopy on the nanometer length scale. *J. Electr. Spectrosc.* **143**, 139–147.

Haguenau, F., Hawkes, P. W., Hutchison, J. L., Satiat-Jeunemaître, B., Simon, G. T., and Williams, D. B. (2003). Key events in the history of electron microscopy. *Microsc. Microanal.* **9**, 96–138.

Haider, M., Rose, H., Uhlemann, S., Kabius, B., and Urban, K. (1998a). Towards 0.1 nm resolution with the first spherically corrected transmission electron microscope. *J. Electr. Microsc.* **47**, 395–405.

Haider, M., Uhlemann, S., Schwan, E., Rose, H., Kabius, B., and Urban, K. (1998b). Electron microscopy image enhanced. *Nature* **392**, 768–769.

Haider, M., Müller, H., Uhlemann, S., Zach, J., Loebau, U., and Hoeschen, R. (2008). Prerequisites for a C_c/C_s-corrected ultrahigh-resolution TEM. *Ultramicroscopy* **108**, 167–178.

Hardy, D. F. (1967). *Combined Magnetic and Electrostatic Quadrupole Electron Lenses.* Ph. D. dissertation, University of Cambridge.

Hartel, P., Rose, H. and Dinges, C. (1996). Conditions and reasons for incoherent imaging in STEM. *Ultramicroscopy* **63**, 93–114.

Hawkes, P. W. (2004). Recent advances in electron optics and electron microscopy. *Annales de la Fondation Louis de Broglie* **29** (Hors série 1), 837–855. Available at http://www.ensmp.fr/aflb/AFLB-295/aflb295m199.pdf.

Hawkes, P. W. (2007). Aberration correction. *In* "Science of Microscopy" (P. W. Hawkes and J. C. H. Spence, eds., Springer, New York and Berlin), pp. 696–747.

Hawkes, P. (2008). Aberrations. *In* "Handbook of Charged Particle Optics," second edition (J. Orloff, ed.). CRC Press, Boca Raton, FL. In press.

Hawkes, P. W., and Kasper, E. (1996). "Principles of Electron Optics," Academic Press, New York, volume 2, pp. 857–863.

Hillier, J., and Ramberg, E. G. (1947). The magnetic electron microscope objective: contour phenomena and the attainment of high resolving power. *J. Appl. Phys.* **18**, 48–71.

Hunt, J. A., Dickerson, F. E., Abbot, A. A., Szantai, G., and Mooney, P. E. (2001). UHV Enfina–a new high-performance EELS spectrometer for the VG STEM. *Microsc. Microanal.* **7** (Suppl 2), 1132–1133.

Hunt, J. A., and Menon, N. K. (2005). Optimizing and Automating EELS/EFTEM parameters using spectrum simulation. *Microsc. Microanal.* **11** (Suppl 2), 490–491.

Isaacson M. and Johnson D. (1975). The microanalysis of light elements using transmitted energy loss electrons. *Ultramicroscopy* **1**, 33–52.

Ishizuka, K. (1994). Coma-free alignment of a high-resolution electron microscope with three-fold astigmatism. *Ultramicroscopy* **55**, 407–418.

Ishizuka, K. (2001). Prospects of atomic resolution imaging with an aberration-corrected STEM. *J. Electr. Microsc.* **50**, 291–305.

Jeanguillaume, C., and Colliex, C. (1989). Spectrum-image: the next step in EELS digital acquisition and processing. *Ultramicroscopy* **28**, 252–257.

Jia, C. L., Lentzen, M., and Urban, K. (2003). Atomic-resolution imaging of oxygen in perovskite ceramics. *Science* **299**, 870–873.

Kahl, F., and Rose, H. (2000). Design of a monochromator for electron sources. *Proc. 12th EUREM Congress (Czechoslovak Society for Electron Microscopy, Brno)* **3**, 459–460.

Kimoto, K., Kothleitner, G., Grogger, W., Matsui, Y., and Hofer, F. (2005). Advantages of a monochromator for bandgap measurements using electron energy-loss spectroscopy. *Micron* **36**, 185–189.

Kimoto, K., Asaka, T., Nagai, T., Saito, M., Matsui, Y., and Ishizuka, K. (2007). Element-selective imaging of atomic columns in a crystal using STEM and EELS. *Nature* **450**, 702–704.

Kimoto, K., Ishizuka, K., and Matsui, Y. (2008). Decisive factors for realizing atomic-column resolution using STEM and EELS. *Micron* **39**, 257–262.

Kirkland, E. J. (1998). "Advanced Computing in Electron Microscopy." Plenum Press, New York.

Kociak, M. (2007). Personal communication.

Koops, H. (1978). Aberration correction in electron microscopy. In "Electron Microscopy" (J. M. Sturgess, ed., Toronto, Microscopical Society of Canada), volume 3, pp. 185–196.

Krivanek, O. L. (1978). EM contrast transfer functions for tilted illumination imaging. In "Electron Microscopy" (J. M. Sturgess, ed., Toronto, Microscopical Society of Canada), volume 1, pp. 168–169.

Krivanek, O. L. (1994). Three-fold astigmatism in high resolution electron microscopy. *Ultramicroscopy* **55**, 419–433.

Krivanek, O. L., Mory, C., Tencé, M., and Colliex, C. (1991). EELS quantification near the single-atom detection level. *Microsc. Microanal. Microstructures* **2**, 257–267.

Krivanek, O. L., and Fan, G. Y. (1992). Complete HREM autotuning using automated diffractogram analysis. In "Proc. 50th EMSA Meeting" (G. W. Bailey, J. Bentley, and J. A. Small, eds., San Francisco Press, San Francisco), pp. 96–97.

Krivanek, O. L., and Mooney, P. E. (1993). Applications of slow-scan CCD cameras in transmission electron microscopy. *Ultramicroscopy* **49**, 95–108.

Krivanek, O. L., and Fan, G. Y. (1994). Application of slow scan CCD cameras to on-line microscope control. *Scanning Microscopy Supplement* **6**, 105–114.

Krivanek, O. L., and Stadelmann, P. A. (1995). Effect of three-fold astigmatism on high resolution electron micrographs. *Ultramicroscopy* **60**, 103–113.

Krivanek, O. L., Kundmann, M. K., and Kimoto, K. (1995). Spatial resolution in EFTEM elemental maps. J. *Microsc.* **180**, 277–287.

Krivanek, O. L., Dellby, N., and Brown, L. M. (1996). Spherical aberration corrector for a dedicated STEM. *Electron Microscopy* (Proceedings EUREM-11, Committee of European Societies of Microscopy, Brussels, 1998) I352–353.

Krivanek, O. L., Dellby, N., Spence, A. J., Camps, R. A., and Brown, L. M. (1997). Aberration correction in the STEM. *In* Inst. Phys. Conf. Ser. (Proceedings 1997 EMAG Meeting, J. M. Rodenburg, ed.), volume 153, pp. 35–40.

Krivanek, O. L., Dellby, N., and Lupini, A. R. (1999). Towards sub-Å electron beams. *Ultramicroscopy* **78**, 1–11.

Krivanek, O. L, Nellist, P. D., Dellby, N., Murfitt, M. F., and Szilagyi, Z. S. (2003). Towards sub-0.5 Å electron beams. *Ultramicroscopy* **96**, 229–237.

Krivanek, O. L., Dellby, N., and Murfitt, M. F. (2008). Aberration correction in electron microscopy. In "Handbook of Charged Particle Optics," second edition. (J. Orloff, ed.). CRC Press, Boca Raton, FL. In press.

Krivanek, O. L., Corbin, G. J., Dellby, N., Elston, B. F., Keyse, R. J., Murfitt, M. F., Own, C. S., Szilagyi, Z. S., and Woodruff, J. W. (2008a). An electron microscope for the aberration-corrected era. *Ultramicroscopy* **108**, 179–195.

Krivanek, O. L., Corbin, G. J., Dellby, N., Murfitt, M., Own, C. S., and Szilagyi, Z. S. (2008b). STEM aberration correction: an integrated approach. *In* "Proceedings 14th European Microscopy Congress" (Meyer J. et al., eds., Springer), vol. **I**, pp. 11–12.

Lazar, S., Botton, G. A., and Zandbergen, H. W. (2006). Enhancement of resolution in core-loss and low-loss spectroscopy in a monochromated microscope. *Ultramicroscopy* **106**, 1091–1103.

Leapman, R. D. (2003). Detecting single atoms of calcium and iron in biological structures by electron energy-loss spectrum-imaging. *J. Microsc.* **210**, 5–15.

Leapman, R. D. (2004). EELS quantitative analysis. *In* "Transmission Electron Energy Loss Spectrometry in Materials Science and The EELS Atlas," second edition (C. C. Ahn, ed., Wiley-VCH Verlag GmbH, Berlin), pp. 49–96.

Leapman, R. D., and Hunt, J. A. (1991). Comparison of detection limits for EELS and EDXS. *Microsc. Microanal. Microstructures* **2**, 231–244.

Lentzen, M. (2006). Progress in aberration-corrected hight-resolution transmission electron microscopy using hardware aberration correction. *Microsc. Microanal.* **12**, 191–205.

Loane, R. F., Xu, P., and Silcox, J. (1991). Thermal vibrations in convergent-beam electron diffraction. *Acta Crystallogr. A* **47**, 267–273.

Martínez, G., and Tsuno, K. (2004). Design of Wien filters with high resolution. *Ultramicroscopy* **100**, 105–114.

Menon, N. K. (2005). EELS Advisor software [Gatan, Inc.]. Available at http://www.gatan.com/software/eels_advisor.php.

Menon, N. K., and Krivanek, O. L. (2002). Synthesis of electron energy loss spectra for the quantification of detection limits. *Microsc. Microanal.* **8**, 203–215.

Mochel, M. E., and Mochel, J. M. (1986). A CCD imaging and analysis system for the VG HB5. *In* "Proc. 44th Annual EMSA Meeting" (G. W. Bailey, ed., San Francisco Press, San Francisco), pp. 616–617.

Möllenstedt, G. (1956). Elektronenmikroskopische bilder mit einem nach O. Scherzer sphärisch korrigierten Objektiv. *Optik* **13**, 2009–2015.

Muller, D. A., and Silcox, J. (1995). Delocalization in inelastic scattering. *Ultramicroscopy* **59**, 195–213.

Muller, D. A., Fitting-Kourkoutis, L., Murfitt, M. F., Song, J. H., Hwang, H. Y., Silcox, J., Dellby, N., and Krivanek, O. L. (2008). Atomic-scale chemical imaging of composition and bonding by aberration-corrected microscopy. *Science* **319**, 1073–1076.

Müller, H., Uhlemann, S., Hartel, P., and Haider, M. (2006). Advancing the hexapole C_s-corrector for the scanning transmission electron microscope. *Microsc. Microanal.* **12**, 442–455.

Nellist, P. D. (2005). Seeing with electrons. *Physics World* **18**, 24–29.

Nellist, P.D., Chisholm, M. F., Dellby, N., Krivanek, O. L., Murfitt, M. F., Szilagyi, Z. S., Lupini, A. R., Borisevich, A., Sides, W. H., and Pennycook, S. J. (2004). Direct sub-ångstrom imaging of a crystal lattice. *Science* **305**, 1741–1742.

Own, C. S., Corbin, G. J., Dellby, N., Elston, B. F., Keyse, R. J., Murfitt, M. F., Szilagyi, Z. S., and Krivanek, O. L. (2006). High-stability, highly automated double-eucentric (S)TEM sample

stage. *Microsc. Microanal.* **12**, 1104–1105CD. [See also http://www.nion.com/tech.html for a film clip showing the operation of the stage.]
Peng, Y., Nellist, P. D., and Pennycook, S. J. (2004). HAADF-STEM imaging with sub-ångstrom probes: a full Bloch-wave analysis. *J. Electr. Microsc.* **53**, 257–266.
Rafferty, B., and Pennycook, S. J. (1999). Towards atomic column by column spectroscopy. *Ultramicroscopy* **78**, 141–151.
Reimer, L. (1995). Electron spectroscopic imaging. *In* "Energy-Filtering Transmission Electron Microscopy" (L. Reimer, ed., Springer, Berlin), pp. 347–400.
Reimer, L. (1997). "Transmission Electron Microscopy," fourth edition, Springer, Berlin, p. 428.
Rose, H. (1981). Correction of aperture aberrations in magnetic systems with threefold symmetry. *Nucl. Instrum. Meth.* **187**, 187–199.
Rose, H. (1990a). Outline of a spherically corrected semiaplanatic medium-voltage transmission electron-microscope. *Optik* **85,** 19–24.
Rose, H. (1990b). Electrostatic energy filter as monochromator of a highly coherent electron source. *Optik* **85**, 95–98.
Rose, H. (2003). Advances in electron optics. *In* "High Resolution Imaging and Spectrometry of Materials" (F. Ernst and M. Rühle, eds., Springer, Berlin), pp. 189–270.
Rose, H. (2004). Outline of an ultracorrector compensating for all primary chromatic and geometrical aberrations of charged-particle lenses. *Nucl. Instrum. Meth. Phys. Res. A* **519**, 12–27.
Sawada, H., Hosokawa, F., Kaneyama, T., Ishizawa, T., Terao, M., Kawazoe, M., Sannomiya, T., Tomita, T., Kondo, Y., Tanaka, T., Oshima, Y., Tanishiro, Y., Yamamoto, N., and Takayanagi, K. (2007). Achieving 63 pm resolution in scanning transmission electron microscope with spherical aberration corrector. *Jap. J. Appl. Phys.* **46**, L568–L570.
Scherzer, O. (1936). Über einige Fehler von Elektronenlinsen. *Z. Physik* **101**, 593–603.
Scherzer, O. (1947). Sphärische und chromatische Korrektur von Elektronenlinsen. *Optik* **2**, 114–132.
Scherzer, O. (1949). The theoretical resolution limit of the electron microscope. *J. Appl. Phys.* **20**, 20–29.
Seeliger, R. (1953). Über die justierung sphärisch korrigierter elektronenoptischer systeme. *Optik* **10**, 29–41.
Shao, Z. (1988). On the fifth order aberration in a sextupole corrected probe forming system. *Rev. Sci. Instrum.* **59**, 2429–2437.
Shao, Z., Beck, V. D., and Crewe, A. V. (1988). A study of octupoles as correctors. *J. Appl. Phys.* **64**, 1646–1651.
Smith, B. W., and Luzzi, D. E. (2001). Electron irradiation effects in single wall carbon nanotubes. *J. Appl. Phys.* **90**, 3509–3515.
Smith, D. J., (2008). Development of Aberration-Corrected Electron Microscopy. *Microsc. Microanal.* **14**, 2–15.
Stone, J. V. (2004). "Independent Component Analysis." MIT Press, Cambridge, MA.
Suenaga, K., Tencé, M., Mory, C., Colliex, C., Kato, H., Okazaki, T., Shinohara, H, Hirahara, K., Bandow, K., Iijima S. (2000). "Element–Selective Single Atom Imaging" *Science* **290**, 2280–2282.
Tencé, M., Quatuccio, M., and Colliex, C. (1995). PEELS compositional profiling and mapping at nanometer spatial resolution. *Ultramicroscopy* **58**, 42–54.
Tencé, M., Pinna, H., Birou, T., Guiraud, G., Mayet, A., Pertel, C., Serin, V., and Colliex. C. (2006). A new detector device designed for quantitative EELS spectroscopy. In "Proc. IMC16," Sapporo, Japan, volume 2, p. 824.
Tiemeijer, P. C. (1999). Operation modes of a TEM monochromator. *Inst. Phys. Conf. Ser.* **161**, 191–194.

Trebbia, P., and Bonnet, N. (1990). EELS elemental mapping with unconventional methods. I. Theoretical basis: image analysis with multivariate and entropy concepts. *Ultramicroscopy* **34**, 165–178.

van Benthem K., Lupini, A. R., Oxley, M. P., Findlay, S. D., Allen, L. J., and Pennycook, S. J. (2006). Three-dimensional ADF imaging of individual atoms by through-focal series scanning transmission electron microscopy. *Ultramicroscopy* **106**, 1062–1068.

van der Stam, M., Stekelenburg, M., Freitag, B., Hubert, D., and Ringnalda, J. (2005). A new aberration-corrected TEM for a new era. *Microscopy and Analysis* **19**, 9–11.

Varela, M., Findlay, S. D., Lupini, A. R., Christen, H. M., Borisevich, A. Y., Dellby, N., Krivanek, O. L., Nellist, P. D., Oxley, M. P., Allen, L. J., and Pennycook, S. J. (2004). Spectroscopic imaging of single atoms within a bulk solid. *Phys. Rev. Lett.* **92**, 095502.

Varela, M., Lupini, A. R., van Benthem, K., Borisevich, A. Y., Chisholm, M. F., Shibata, N., Abe E., and Pennycook, S. J. (2005). Materials characterization in the scanning transmission electron microscope. *Ann. Rev. Mater. Res.* **35**, 539–569.

Watanabe, M., Ackland, D. W., Burrows, A., Kiely, C. J., Williams, D. B., Krivanek, O. L., Dellby, N., Murfitt, M. F., and Szilagyi, Z. (2006). Improvements in the X-ray analytical capabilities of a scanning transmission electron microscope by spherical-aberration correction. *Microsc. Microanal.* **12**, 515–526.

Watanabe, M., Kanno, M., Ackland, D.W., Kiely, C. J., and William, D. B. (2007). Application of electron energy-loss spectrometry and energy filtering in an aberration-corrected JEM-2200FS STEM/TEM. *Microsc. Microanal.* **13** (Suppl 2), 1264–1265 CD.

Zach, J., and Haider, M. (1995a). Correction of spherical and chromatic aberration in a low–voltage SEM. *Optik* **99**, 112–118.

Zach, J., and Haider, M. (1995b). Aberration correction in a low-voltage SEM by a multipole corrector. *Nucl. Instr. Meth. A* **363**, 316–325.

Zemlin, F., Weiss, K., Schiske, P., Kunath, W., and Herrmann, K. H. (1978). Coma-free alignment of high resolution electron microscopes with the aid of optical diffractograms. *Ultramicroscopy* **3**, 49–60.

Zobelli, A., Gloter, A., Ewels, C. P., Seifert, G., and Colliex, C. (2007). Electron knock-on cross section of carbon and boron nitride nanotubes. *Phys. Rev. B* **75**, 245402.

Zworykin, V. K., Morton, G. A., Ramberg, E. G., Hillier, J., and Vance, W. A. (1945). "Electron Optics and the Electron Microscope," Wiley, New York, pp. 630–633.